



Immobilization of facet-engineered Ag_3PO_4 on mesoporous Al_2O_3 for efficient industrial waste gas purification with indoor LED illumination

Dehua Xia^{a,b,*}, Lingling Hu^a, Yunchen Wang^a, Bohong Xu^a, Yuhong Liao^a, Chun He^{a,*}, Liqun Ye^c, Xiaoliang Liang^d, Yinghao Ye^e, Dong Shu^f

^a School of Environmental Science and Engineering, Sun Yat-sen University, Guangzhou, 510275, China

^b Guangdong Provincial Key Laboratory of Environmental Pollution Control and Remediation Technology, Guangzhou, 510275, China

^c College of Materials and Chemical Engineering, Key Laboratory of Inorganic Nonmetallic Crystalline and Energy Conversion Materials, China Three Gorges University, Yichang, 443002, China

^d CAS Key Laboratory of Mineralogy and Metallogeny and Guangdong Provincial Key Laboratory of Mineral Physics and Materials, Guangzhou Institute of Geochemistry, Chinese Academy of Sciences, Guangzhou, 510640, China

^e The Center of New Energy Materials and Technology, School of Materials Science and Engineering, Southwest Petroleum University, Chengdu, 610500, China

^f Key Lab of Technology on Electrochemical Energy Storage and Power Generation in Guangdong Universities, School of Chemistry and Environment, South China Normal University, Guangzhou, 510006, China

ARTICLE INFO

Keywords:

Adsorption energy

In situ FT-IR

Facet-dependent effect

Interfacial charge separation

Silver phosphate

ABSTRACT

The immobilization of a photocatalyst on a proper support is pivotal for practical environmental applications. Herein, as a rising visible light photocatalyst, different facet-engineered $\text{Ag}_3\text{PO}_4\{111\}$, $\text{Ag}_3\text{PO}_4\{110\}$, $\text{Ag}_3\text{PO}_4\{100\}$ and irregular Ag_3PO_4 were first immobilized on mesoporous Al_2O_3 , then applied for photocatalytic removal of ppm-leveled NO under visible light illumination. Photocatalytic performances for NO removal by these immobilized Ag_3PO_4 were found to be highly facet-dependent, showing the degradation kinetics in the order of $\text{Ag}_3\text{PO}_4\{111\}$ tetrahedra > $\text{Ag}_3\text{PO}_4\{110\}$ rhombic dodecahedra > $\text{Ag}_3\text{PO}_4\{100\}$ cubes > irregular Ag_3PO_4 . The density functional theory (DFT) calculations were used to investigate the difference in the catalytic activity of $\text{Ag}_3\text{PO}_4/\text{Al}_2\text{O}_3$ with exposed $\{111\}$, $\{110\}$, and $\{100\}$ facets. The experimental characterization and theoretical calculations all confirm that the $\{111\}$ facets with high surface energy can not only facilitate adsorption/activation of O_2 and H_2O but also be beneficial to the generation of $\cdot\text{O}_2^-$ and $\cdot\text{OH}$ radicals, which result in significantly enhanced activity for NO oxidation. A modified band diagram showing different degrees of band edge bending can explain these observations. A reaction pathway study based on both *in situ* FT-IR and molecular-level simulation of NO adsorption and transformation indicates that this $\text{Ag}_3\text{PO}_4\{111\}/\text{Al}_2\text{O}_3$ can efficiently adsorb NO and transform it into harmless nitrate products via $\text{NO} \rightarrow \text{NO}^+$ and $\text{NO}_2^+ \rightarrow \text{nitrate}$ or nitrite routes. The present work reveals the facet-dependent radical formation mechanisms of $\text{Ag}_3\text{PO}_4/\text{Al}_2\text{O}_3$, and also provides new perspectives for promoting environmental applications of immobilized photocatalysts.

1. Introduction

Nitric oxide (NO) and nitrogen dioxides (NO_2), commonly named as NO_x , are typical air pollutants with increasing environmental concern [1]. NO_x is mainly generated from the combustion of fossil fuel, and its concentration in the atmosphere has greatly increased in recent decades due to the increased automobiles and industrial activities [2]. NO_x is one of the major contributors to acid rain, photochemical smog, and haze, which could cause serious respiratory diseases, heart or lung diseases [3–5]. For NO_x from industrial emissions, conventional techniques (such as adsorption, biofiltration, selected catalytic reduction,

and thermal catalysis reduction) could function well for high concentration of NO_x , but they are not economically feasible for NO_x elimination at the lower parts per million (ppm) level in industrial waste gas [6,7]. Therefore, the ideal technology for these cases should be developed with further decreasing the costs.

Photocatalytic process, as a green technology that could use natural sunlight or artificial light to purify air of low concentration under mild conditions, providing an attractive alternative to conventional approaches [8,9]. Till now, several visible-light-driven (VLD) photocatalysts have been prepared and applied for NO_x removal, such as ZnFe_2O_4 , Bi_2WO_6 , Bi, $\text{In}(\text{OH})_x\text{S}_y$, hematite, and $\text{Bi-C}_3\text{N}_4$, etc. [10–15].

* Corresponding authors at: School of Environmental Science and Engineering, Sun Yat-sen University, Guangzhou, 510275, China.

E-mail addresses: xiadehua3@mail.sysu.edu.cn (D. Xia), hechun@mail.sysu.edu.cn (C. He).

<https://doi.org/10.1016/j.apcatb.2019.117811>

Received 25 February 2019; Received in revised form 11 May 2019; Accepted 1 June 2019

Available online 03 June 2019

0926-3373/© 2019 Elsevier B.V. All rights reserved.

All these visible-light-driven photocatalysts have exhibited great performances for NO_x removal. However, these well-studied photocatalysts are usually in powder form without immobilization, and studies are only limited in indoor air with ppb-leveled NO_x . For practical application, the photocatalysts in powder form would be simply blown away, causing lower removal efficiency and difficulty in separation. To eliminate the nano-photocatalysts blown away effect, it is essential to develop a facile process to effectively immobilize the nano-photocatalysts on a proper support before utilization. Meanwhile, to further promote the photocatalysis for air purification, it is needed to search for other alternative photocatalyst with higher activity.

Recently, silver-based oxides Ag_3PO_4 has attracted intensive interests because of its promising applications in solar energy conversion and environmental remediation [16,17]. Attributed to its scattered band structure and accelerated electron-hole separation, the quantum efficiency of Ag_3PO_4 can reach up to 90% under visible light irradiation [18]. Specially, recent research advances have revealed that manipulating the exposed facets on Ag_3PO_4 crystal surfaces will lead to a dramatic change in reactivity, because different facets of a given crystalline have different structural and electronic properties [19]. It is widely accepted in photocatalysis that a higher surface energy leads to a more reactive surface. For instance, Bi et al. has identified the surface energy of $\text{Ag}_3\text{PO}_4\{111\}$ (1.65 J m^{-2}) was much higher than that of $\text{Ag}_3\text{PO}_4\{110\}$ (0.78 J m^{-2}) and $\text{Ag}_3\text{PO}_4\{100\}$ (0.67 J m^{-2}), thus inducing 10 times of oxygen evolution for $\text{Ag}_3\text{PO}_4\{111\}$ than other two facets [20]. Other mechanisms have also been proposed to explain the facet-dependent catalytic activities. For example, Zheng et al. proposed that the photocatalytic activity of the facets is related to its band gap; with largest band gap (2.736 eV), the photogenerated electrons and holes on the $\text{Ag}_3\text{PO}_4\{110\}$ surface is likely to possess higher energy and activity, and thus accounts for the highest photocatalytic activity [21]. However, Hsieh et al. reported that $\text{Ag}_3\text{PO}_4\{100\}$ cubes are more photocatalytically active than rhombic dodecahedra $\{110\}$ toward photodegradation of methyl orange, and tetrahedra $\{111\}$ are inactive. Because the $\{111\}$ surface is drawn to bend up most steeply and deviate from the normal band positions to indicate the highest barrier for electron transport to the crystal surface [22]. Clearly, the origin of facet-dependent photocatalytic activity is not fully understood and need to be further identified. In addition to the above-mentioned mechanisms, we speculated that the facet-dependent radical formation mechanisms are also a critical mechanism resulting in the observed facet-dependent catalytic activities, since reactive species measurements have not been performed on single Ag_3PO_4 crystals.

Motivated by the good performance of Ag_3PO_4 , it is promising to immobilize facet engineered Ag_3PO_4 on a proper support and utilize to eliminate NO_x . Moreover, the facet-dependent photocatalytic mechanism for NO_x removal with Ag_3PO_4 is still unknown. In this study, three different facet engineered Ag_3PO_4 and irregular Ag_3PO_4 were effectively immobilized on mesoporous Al_2O_3 through an *in-situ* impregnation-precipitation method. We observed that the $\text{Ag}_3\text{PO}_4\{111\}$ facets exhibited a much higher photocatalytic activity in the degradation of NO under visible light than the $\{110\}$ and $\{100\}$ facets. The theoretical calculation using density functional theory (DFT), electron spin resonance spectroscopy, and radical scavenging experiments were carried out to understand the interactions of the $\{111\}$, $\{110\}$ and $\{100\}$ facets with $\text{O}_2/\text{H}_2\text{O}$ and different types/amounts of free radicals generated. The mechanisms controlling the observed facet-dependent photocatalytic activities were proposed. Furthermore, to test the applicability of $\text{Ag}_3\text{PO}_4\{111\}/\text{Al}_2\text{O}_3$, different parameters like supporters, calcination temperature, photocatalyst amount, inlet gas flow, and the stability were also evaluated. The present investigation demonstrated that $\text{Ag}_3\text{PO}_4/\text{Al}_2\text{O}_3$ was efficient for NO purification at ppm-level in industrial waste gas, which could promote the environmental application of an efficient photocatalyst.

2. Experimental methods

2.1. Immobilization of facet engineered Ag_3PO_4 on mesoporous Al_2O_3

In a typical process, different facet engineered and irregular Ag_3PO_4 were immobilized on mesoporous Al_2O_3 through an *in situ* wet impregnation-precipitation method. (1) Preparation of $\text{Ag}_3\text{PO}_4\{111\}$ tetrahedra/ Al_2O_3 : 2 g AgNO_3 and 2.5 mL 85% H_3PO_4 were respectively solute into 80 mL ethanol to prepare solution A. Later, in the 60 °C water bath, 50 g Al_2O_3 particles were impregnated into H_3PO_4 solution with constant stirring for 30 min, then solution A was dropwise added and maintained for 6 h, thus to form $\text{Ag}_3\text{PO}_4\{111\}/\text{Al}_2\text{O}_3$; (2) Preparation of $\text{Ag}_3\text{PO}_4\{110\}$ rhombic dodecahedra/ Al_2O_3 : 50 g Al_2O_3 particles were impregnated into 0.4175 g CH_3COOAg solution with constant stirring for 30 min. Later, 0.00085 M $\text{Na}_2\text{HPO}_4\text{-Na}_3\text{PO}_4$ (1:1) was dropwise added into above mixture and maintained for 6 h, thus to form $\text{Ag}_3\text{PO}_4\{110\}/\text{Al}_2\text{O}_3$; (3) $\text{Ag}_3\text{PO}_4\{100\}$ cube/ Al_2O_3 : 50 g Al_2O_3 particles were impregnated into 0.05 M AgNO_3 solutions with constant stirring for 30 min, then 0.1 M ammonia was dropwise added into above solution, thus to form into a transparent $\text{Ag}(\text{NH}_3)_2\text{OH}$ mixture. Later, 0.03 M $\text{Na}_2\text{HPO}_4\cdot 12\text{H}_2\text{O}$ was dropwise added into above mixture and maintained for 6 h, thus to form $\text{Ag}_3\text{PO}_4\{100\}/\text{Al}_2\text{O}_3$; (4) irregular $\text{Ag}_3\text{PO}_4/\text{Al}_2\text{O}_3$: 50 g Al_2O_3 particles were impregnated into 0.05 M AgNO_3 solutions with constant stirring for 30 min, then 0.03 M $\text{Na}_2\text{HPO}_4\cdot 12\text{H}_2\text{O}$ was dropwise added into above mixture and maintained stirring for another 30 min, thus the precipitated Ag^+ ions would react with PO_4^{3-} to form irregular $\text{Ag}_3\text{PO}_4/\text{Al}_2\text{O}_3$. Finally, the resulting samples were washed several times with deionized water and dried at 80 °C for 12 h in oven [19–22].

To make a comparison, other different mesoporous supports like Zeolite Socony Mobil-5A (ZSM-5A), ZSM-4A, and zeolite were also utilized to immobilize $\text{Ag}_3\text{PO}_4\{111\}$ with same method like $\text{Ag}_3\text{PO}_4\{111\}/\text{Al}_2\text{O}_3$. To study the effect of calcination temperature to photocatalytic activity, the $\text{Ag}_3\text{PO}_4\{111\}/\text{Al}_2\text{O}_3$ photocatalysts were calcined at 200 °C, 300 °C, 400 °C, 500 °C for 3 h in furnace. All chemicals with analytical grade were purchased from Guangdong Guanghua Chemical Co., Ltd. China. Activated aluminium oxide (Al_2O_3) was purchased from Sinopharm Chemical Reagent Co., Ltd.

2.2. Characterization of facet engineered $\text{Ag}_3\text{PO}_4/\text{Al}_2\text{O}_3$ photocatalyst

The morphology of as-prepared $\text{Ag}_3\text{PO}_4/\text{Al}_2\text{O}_3$ was observed through scanning electron microscope (SEM, JEOL). The crystal phase of as-prepared $\text{Ag}_3\text{PO}_4/\text{Al}_2\text{O}_3$ was analyzed by X-ray diffraction (XRD, D-MAX 2200 VPC Japan) with radiation of Cu target (K_α , $\lambda = 1.54059 \text{ \AA}$). Raman spectra were recorded using a micro-Raman spectrometer (Renishaw InVia) in the back scattering geometry with a 514.5 nm Ar^+ laser as an excitation source. The element contents of as-prepared photocatalysts were determined by energy-dispersive spectroscopy (EDS, JEOL). The surface properties of as-prepared $\text{Ag}_3\text{PO}_4/\text{Al}_2\text{O}_3$ were analyzed on X-ray photoelectron spectroscopy (XPS, Perkin-Elmer PHI-5600ci) with the $\text{AlK}\alpha$ line at 100 W. UV-vis diffuse reflectance spectra (UV-vis DRS) of as-prepared $\text{Ag}_3\text{PO}_4/\text{Al}_2\text{O}_3$ was recorded on a spectrophotometer (Shimadzu UV-PC3101PC) with an integrating sphere (Specular reflectance ATT.5DEG). The electrochemical impedance spectroscopy (EIS) measurements were carried out using a potentiostat/galvanostat (Autolab, PGSTAT302N) coupled to a lock-in amplifier. Nitrogen adsorption-desorption isotherms were obtained on a nitrogen adsorption apparatus (Quantachrome, USA) with samples degassed at 300 °C for 12 h prior to measurements.

2.3. Visible-light-driven photocatalytic removal of NO

The photocatalytic removal of NO at ppm-levels by facet engineered $\text{Ag}_3\text{PO}_4/\text{Al}_2\text{O}_3$ was carried out in a photocatalytic reactor at ambient condition (Fig. S1). The photocatalytic reactor was made of Pyrex glass

with a size of 2.0 cm in diameter and 60 cm in height. A 10 W white LED tube (Shanghai Aojia Lighting Appliance Co. Ltd.), was vertically placed inside the reactor, whose light spectrum was shown in Fig. S2. The initial concentration of inlet NO was diluted to be 50 ppm by the air stream, then pumped into the photocatalytic reactor through a sparger with the inlet velocity was controlled at 0.15 L min^{-1} by a mass flow controller. Two NO sensors (S_1 , S_2) (Detcon, DM-100-NO) were installed to continuously monitor the inlet and outlet of NO concentration. For each experiment, $\text{Ag}_3\text{PO}_4/\text{Al}_2\text{O}_3$ samples were previously padded in the reactor, after the adsorption-desorption equilibrium between NO and photocatalysts was achieved, the white LED tube was turned on. The NO removal efficiency (η) was calculated as Eq. 1.

$$\eta (\%) = (1 - C/C_0) \times 100\% \quad (1)$$

Where C and C_0 were concentrations of NO in the outlet stream and inlet stream, respectively.

2.4. Scavenger experiments and analytical methods

Different chemical scavengers were added into photocatalytic reactor to trap specific reactive species. Scavenger stock solutions: 1.0 M isopropanol (Riedel-de Haën®, Germany) for $\cdot\text{OH}$, 1.0 M $\text{K}_2\text{Cr}_2\text{O}_7$ (Merck, Germany) for e^- , 1.0 M sodium oxalate (Fuchen, China) for h^+ , 0.1 M TEMPOL (Fuchen, China) for $\cdot\text{O}_2^-$, 0.1 M NaN_3 (Fuchen, China) for $^1\text{O}_2$ [23]. The electron spinning resonance (ESR) measurement (FLsp920, U.K.) was prepared by mixing different facet engineered $\text{Ag}_3\text{PO}_4/\text{Al}_2\text{O}_3$ in a 50 mM DMPO solution with aqueous dispersion for DMPO- $\cdot\text{OH}$ and methanol dispersion for DMPO- $\cdot\text{O}_2^-$ [24]. The tail gas absorption solution was determined by Dionex ICS-90 ion chromatography (IC) with an anion column (IonPac AS14A4-250 mm). Chromatographic conditions: flow rate (0.80 mL min^{-1}), injection volume ($20 \mu\text{L}$), column temperature (303 K), eluent ($1.8 \text{ mM Na}_2\text{CO}_3 + 4.5 \text{ mM NaHCO}_3$), and automatic regeneration suppression system ($45 \text{ mM H}_2\text{SO}_4$) [25].

pCBA is a well-known specific probe to detect $\cdot\text{OH}$ due to its high reactivity with $\cdot\text{OH}$ ($k_{\text{OH}, \text{pCBA}} = 5.2 \times 10^9 \text{ M}^{-1} \text{ s}^{-1}$), the concentration of $[\cdot\text{OH}]_{\text{ss}}$ (steady state $\cdot\text{OH}$) can be quantified following Eq. 2. The decay of pCBA in the collected filtrate was analyzed with a high performance liquid chromatography system (Dionex U3000, Sunnyvale, CA) equipped with a Thermo Scientific Hypersil BDS C18 column [26].

$$-\ln ([\text{pCBA}]/[\text{pCBA}]_0) = k_{\text{OH}, \text{pCBA}} \times [\cdot\text{OH}] \times t \quad (2)$$

Where $[\text{pCBA}]$ and $[\text{pCBA}]_0$ ($20 \mu\text{M}$) were concentrations of residual and initial pCBA, respectively.

$\cdot\text{O}_2^-$ has high reactivity with nitro blue tetrazolium (NBT, $k_{\text{O}_2, \text{NBT}} = 5.88 \times 10^4 \text{ M}^{-1} \text{ s}^{-1}$), the concentration of $[\cdot\text{O}_2^-]_{\text{ss}}$ can be quantified following Eq. 3. The decrease in the concentration of NBT can be measured on a UV-vis spectrophotometer (LabTech) at a wavelength of 259 nm [26].

$$-\ln ([\text{NBT}]/[\text{NBT}]_0) = k_{\text{O}_2, \text{NBT}} \times [\cdot\text{O}_2^-] \times t \quad (3)$$

Where $[\text{NBT}]$ and $[\text{NBT}]_0$ (0.15 mM) were concentrations of residual and initial NBT, respectively.

2.5. In situ DRIFTS investigation

In situ DRIFTS measurements were conducted using a TENSOR II FT-IR spectrometer (Bruker) equipped with an *in situ* diffuse reflectance cell (Harrick) and a high-temperature reaction chamber (HVC). The reaction chamber was equipped with three gas ports and two coolant ports. High purity N_2 , O_2 and 50 ppm of NO mixture could be fed into the reaction system, and a three-way ball valve was used to switch between the target gas (NO) and purge gas (N_2). The total gas flow rate was 100 mL/min , and the concentration of NO was adjusted to 50 ppm by dilution with N_2 . The chamber was enclosed with a dome having

three windows, two for IR light entrance and detection, and one for illuminating the photocatalyst. The observation window was made of UV quartz and the other two windows were made of ZnSe. A Xe lamp (MVL-210, Optpe, Japan) was used as the irradiation light source.

2.6. Theoretical calculations

The first-principle calculations were performed by VASP code with PBE function. Both the atomic positions and lattice constants were optimized for Ag_3PO_4 with the $\{111\}$, $\{110\}$ and $\{100\}$ facets. The projector-augmented wave method was used with a plane-wave basis [27]. The cutoff energy and Gaussian smearing width were respectively set to 500 eV and 0.2 eV . The Brillouin zone was sampled with a $5 \times 5 \times 1 \text{ K}$ points. All structures and energy are allowed to relax below $0.01 \text{ eV } \text{\AA}^{-1}$.

The surface energy (γ) of surface slabs is defined and calculated as follows:

$$\gamma = \frac{E_s - nE_b}{2A} \quad (4)$$

Where E_s is the energy of a slab containing n formula units and E_b is the total energy per formula unit of bulk Ag_3PO_4 . A is the area of the slab surface, and the factor of 2 reflects the fact that there are two surfaces for each slab.

To understand the absorptive properties of those surface slabs, an additional molecule is allowed to adsorb on the surface, and its adsorption energy (E_{ads}) is calculated from the formula:

$$E_{\text{ads}} = E_{\text{total}} - E_{\text{basic}} - E_{\text{molecule}} \quad (5)$$

Where E_{ads} is adsorption energy of oxygen or water molecule; E_{total} , E_{basic} , and E_{molecule} are the total energy of the surface containing the adsorbate, of a clean surface, and of an isolated molecule, respectively.

3. Results and discussion

3.1. Facet-dependent microstructures of $\text{Ag}_3\text{PO}_4/\text{Al}_2\text{O}_3$

Fig. 1 depicted the photos of as-prepared different facet engineered $\text{Ag}_3\text{PO}_4/\text{Al}_2\text{O}_3$ products. Clearly, the colour was changed from white to yellow after Ag_3PO_4 deposition. The microstructures of the as-prepared $\text{Ag}_3\text{PO}_4/\text{Al}_2\text{O}_3$ samples were also observed by SEM, it can be seen that Ag_3PO_4 particles were well dispersed on the surface of Al_2O_3 . Fig. 1a shows that the surface of $\text{Ag}_3\text{PO}_4\{111\}/\text{Al}_2\text{O}_3$ surface is fully characterized with four triangle $\{111\}$ facets, with average sizes of $0.52 \mu\text{m}$ tetrahedra in a high yield. In Fig. 1b, the surface of $\text{Ag}_3\text{PO}_4\{110\}/\text{Al}_2\text{O}_3$ is in regular rhombic dodecahedral morphology with average size of $0.5 \mu\text{m}$, and their sub-microcrystals are enclosed by twelve well-defined $\{110\}$ planes with single-crystal structure. In Fig. 1c, sub-microcubes of $\text{Ag}_3\text{PO}_4\{100\}/\text{Al}_2\text{O}_3$ surface are uniform with smooth surfaces, sharp corners and edges, which are completely bounded by six square $\{100\}$ facets. In contrast, Fig. 1d indicates that microstructures of irregular $\text{Ag}_3\text{PO}_4/\text{Al}_2\text{O}_3$ surface are in irregular sphere, whose particle size is estimated to be around 250 nm .

The XRD patterns of all the $\text{Ag}_3\text{PO}_4/\text{Al}_2\text{O}_3$ are shown in Fig. 2a, except for the substrate peaks of Al_2O_3 , the major diffraction peaks could be well indexed to the body-centered cubic structure of Ag_3PO_4 (JCPDS No.06-0505), indicating the formation of single crystalline phase of Ag_3PO_4 . Moreover, the diffraction patterns of different facet engineered $\text{Ag}_3\text{PO}_4/\text{Al}_2\text{O}_3$ exhibit variations in intensity ratios. Tetrahedral $\text{Ag}_3\text{PO}_4\{111\}/\text{Al}_2\text{O}_3$ has an intensity ratio of 2.91 between $\{222\}$ and $\{200\}$ planes, while the rhombic dodecahedron, cubic, spherical structures have an approximate ratio of 1.05, confirming that tetrahedral particles are mainly bounded of $\text{Ag}_3\text{PO}_4\{111\}$ crystalline planes [20–22]. Furthermore, in contrast with the intensity ratio between $\{110\}$ and $\{200\}$ for irregular $\text{Ag}_3\text{PO}_4/\text{Al}_2\text{O}_3$ is 0.68, rhombic dodecahedral $\text{Ag}_3\text{PO}_4\{110\}/\text{Al}_2\text{O}_3$ has an obviously higher value of

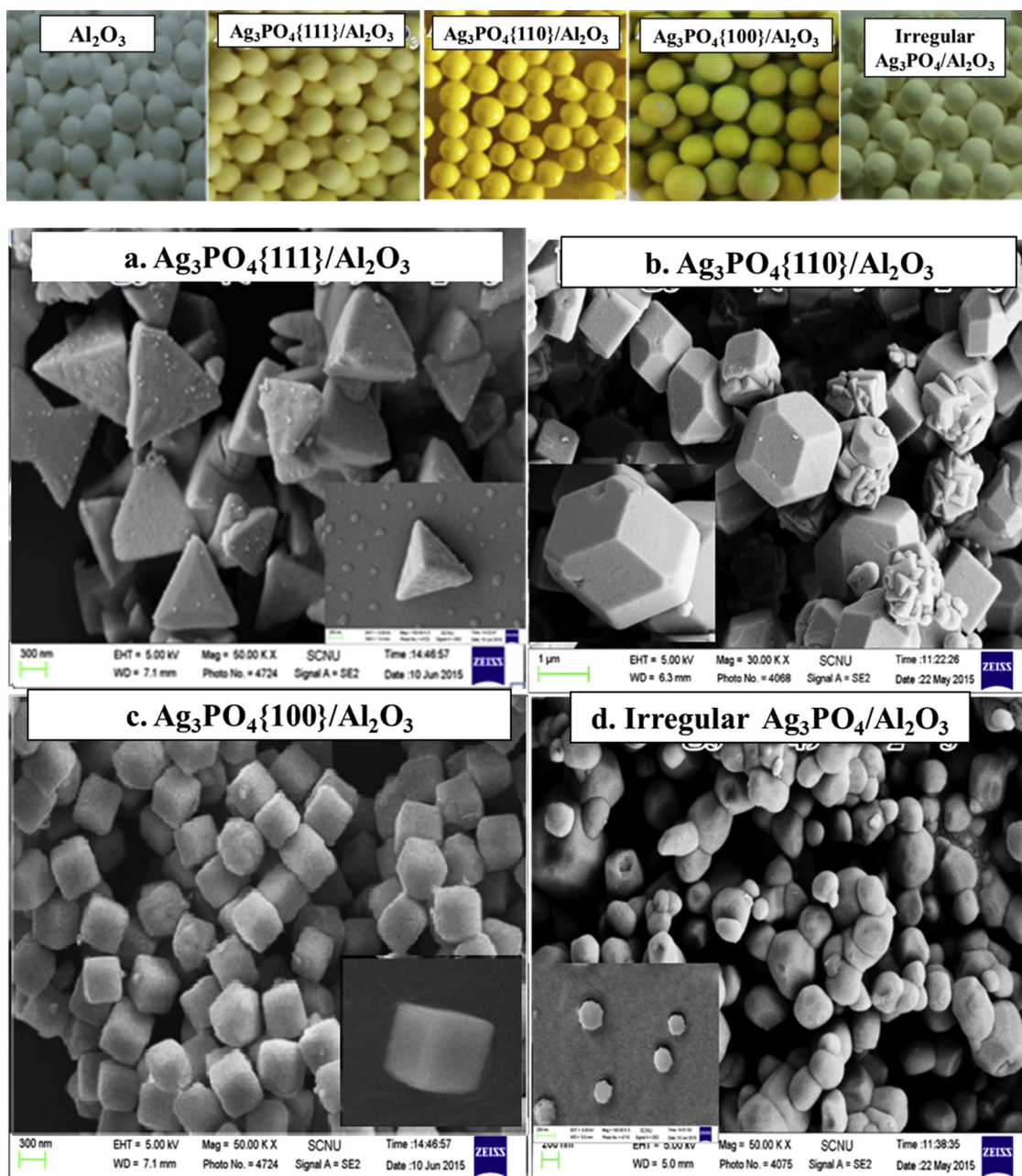


Fig. 1. Photos and SEM images of as-prepared (a) tetrahedral{111}, (b) rhombic dodecahedral{110}, (c) cubic {100}, and (d) irregular Ag_3PO_4 sub-microcrystals deposited on mesoporous Al_2O_3 .

1.83 and cubic $\text{Ag}_3\text{PO}_4\{100\}/\text{Al}_2\text{O}_3$ has a lower value of only 0.61, confirming as previously reported rhombic dodecahedrons and cubic crystal structures are primarily bounded with {110} and {100} planes, respectively [20–22].

In order to analyze the vibration features of different facet engineered $\text{Ag}_3\text{PO}_4/\text{Al}_2\text{O}_3$, Raman analysis were performed and shown in Fig. 2b. Clearly, all the $\text{Ag}_3\text{PO}_4/\text{Al}_2\text{O}_3$ samples exhibit same patterns, consistent with other studies [27]. Based on the group theory analysis, the band at 215 cm^{-1} is attributed to the external modes; the weak peak at 400 cm^{-1} is ascribed to the bending vibration of the tetrahedral PO_4 ionic group; two broad Raman shifts centered at 555 cm^{-1} and 710 cm^{-1} are due to the symmetric stretch of P–O–P bonds; the higher wavenumber band locates at 905 cm^{-1} is corresponding to the motion of terminal oxygen bond vibrations in phosphate chains; and the broad peak at 1001 cm^{-1} is assigned to the symmetric stretch of O–P–O bonds [27,28]. Obviously, the intensity for $\text{Ag}_3\text{PO}_4\{111\}/\text{Al}_2\text{O}_3$ are

much stronger than other that of other facets, suggesting $\text{Ag}_3\text{PO}_4\{111\}/\text{Al}_2\text{O}_3$ may contain more defects or vacancies on their crystalline face [29]. These vacancies could affect the charge transfer and separation process, thus would play an important role in the photocatalytic activities of $\text{Ag}_3\text{PO}_4\{111\}/\text{Al}_2\text{O}_3$.

The elemental composition and chemical status of different facet engineered $\text{Ag}_3\text{PO}_4/\text{Al}_2\text{O}_3$ were further investigated by XPS analysis. The XPS peaks in Fig. 2c showed the main peaks of $\text{Ag}3d$, $\text{P}2p$, $\text{O}1s$, $\text{Al}2p$, confirming the coexistence of Ag, P, O, Al. Moreover, the obtained atom ratios of Ag and P (2.91: 1) were fitted well to the chemical formula of Ag_3PO_4 , also consistent with the EDS analysis (Ag: P = 2.83: 1) in Fig. S3, further confirming the coexistence of Ag_3PO_4 and Al_2O_3 . Furthermore, the two characteristic peaks of Ag 3d signal have been further deconvoluted and shown in Fig. 2d. The two broad peaks located at 367.5 and 373.6 eV can be assigned to the doublet Ag $3d_{5/2}$ and Ag $3d_{3/2}$, which are typical values for Ag^+ in Ag_3PO_4 , indicating there

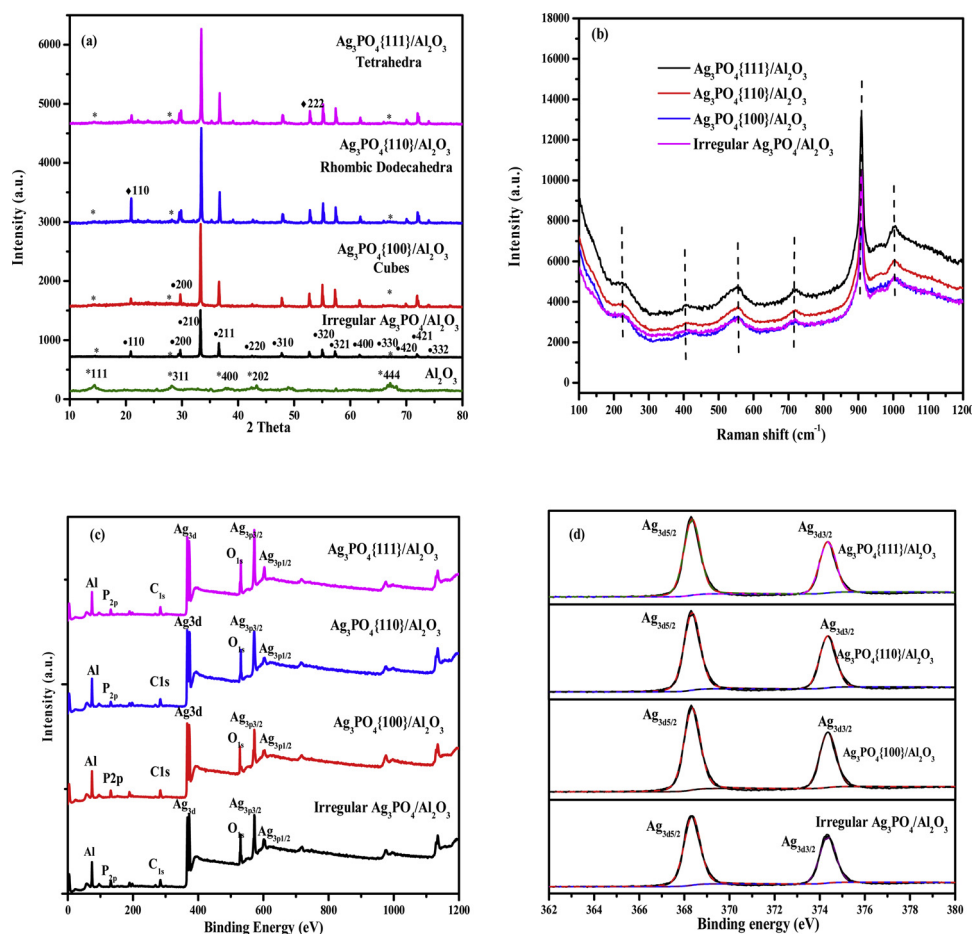


Fig. 2. (a) XRD patterns (b) Raman spectra, (c) XPS spectra; and (d) High resolution XPS spectra of Ag 3d of as-prepared $\text{Ag}_3\text{PO}_4\{111\}/\text{Al}_2\text{O}_3$, $\text{Ag}_3\text{PO}_4\{110\}/\text{Al}_2\text{O}_3$, $\text{Ag}_3\text{PO}_4\{100\}/\text{Al}_2\text{O}_3$ and irregular $\text{Ag}_3\text{PO}_4/\text{Al}_2\text{O}_3$.

is no formation of Ag nanoparticles [30]. Therefore, with the combination of the XRD, SEM, Raman, EDS and XPS investigation, the results confirmed that both Ag_3PO_4 and Al_2O_3 species were contained in the as-prepared photocatalysts.

Moreover, N_2 adsorption/desorption isotherms were utilized to further analyze the pore-size distribution and mesoporous architecture of the pristine Al_2O_3 , $\text{Ag}_3\text{PO}_4\{111\}/\text{Al}_2\text{O}_3$, $\text{Ag}_3\text{PO}_4\{110\}/\text{Al}_2\text{O}_3$, $\text{Ag}_3\text{PO}_4\{100\}/\text{Al}_2\text{O}_3$ and irregular $\text{Ag}_3\text{PO}_4/\text{Al}_2\text{O}_3$ samples. As shown in Fig. 3a, both plots display a type-IV isotherm being representative of

mesoporous materials. After $\text{Ag}_3\text{PO}_4\{111\}$, $\text{Ag}_3\text{PO}_4\{110\}$, $\text{Ag}_3\text{PO}_4\{100\}$ and irregular Ag_3PO_4 deposited on mesoporous Al_2O_3 , the specific surface area of pristine Al_2O_3 decreased from 251.4 to $184.0 \text{ m}^2 \text{ g}^{-1}$, $193.2 \text{ m}^2 \text{ g}^{-1}$, $182.1 \text{ m}^2 \text{ g}^{-1}$ and $163.8 \text{ m}^2 \text{ g}^{-1}$, respectively, while the pore volume also decreased from 29.8 to $26.6 \text{ cm}^3 \text{ g}^{-1}$, $26.9 \text{ cm}^3 \text{ g}^{-1}$, $26.1 \text{ cm}^3 \text{ g}^{-1}$ and $25.4 \text{ cm}^3 \text{ g}^{-1}$, indicating that all Ag_3PO_4 particles were highly dispersed on Al_2O_3 surface and even embedded into the inner channel of Al_2O_3 (Fig. 3b). Actually, the mesoporous architecture of Al_2O_3 provides large surface area and pore

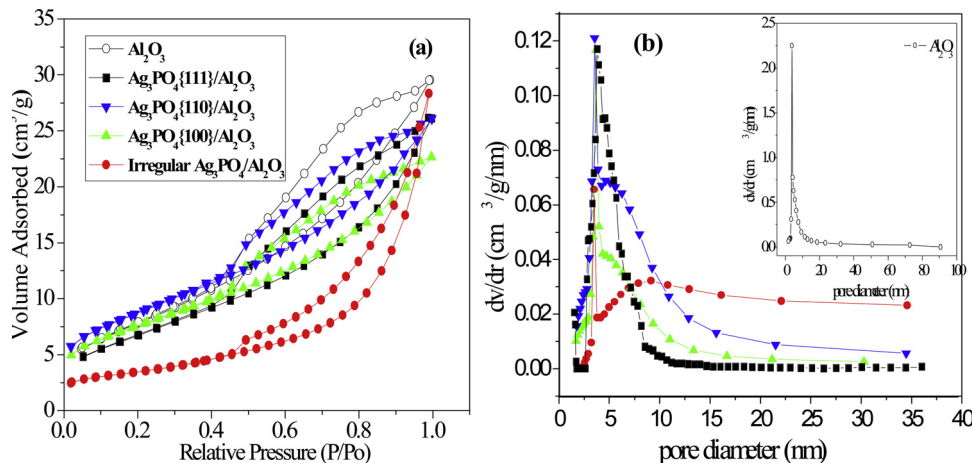


Fig. 3. (a) N_2 adsorption and desorption isotherms and (b) corresponding pore-size distribution curves for $\text{Ag}_3\text{PO}_4\{111\}/\text{Al}_2\text{O}_3$, $\text{Ag}_3\text{PO}_4\{110\}/\text{Al}_2\text{O}_3$, $\text{Ag}_3\text{PO}_4\{100\}/\text{Al}_2\text{O}_3$, irregular $\text{Ag}_3\text{PO}_4/\text{Al}_2\text{O}_3$ samples and pristine Al_2O_3 .

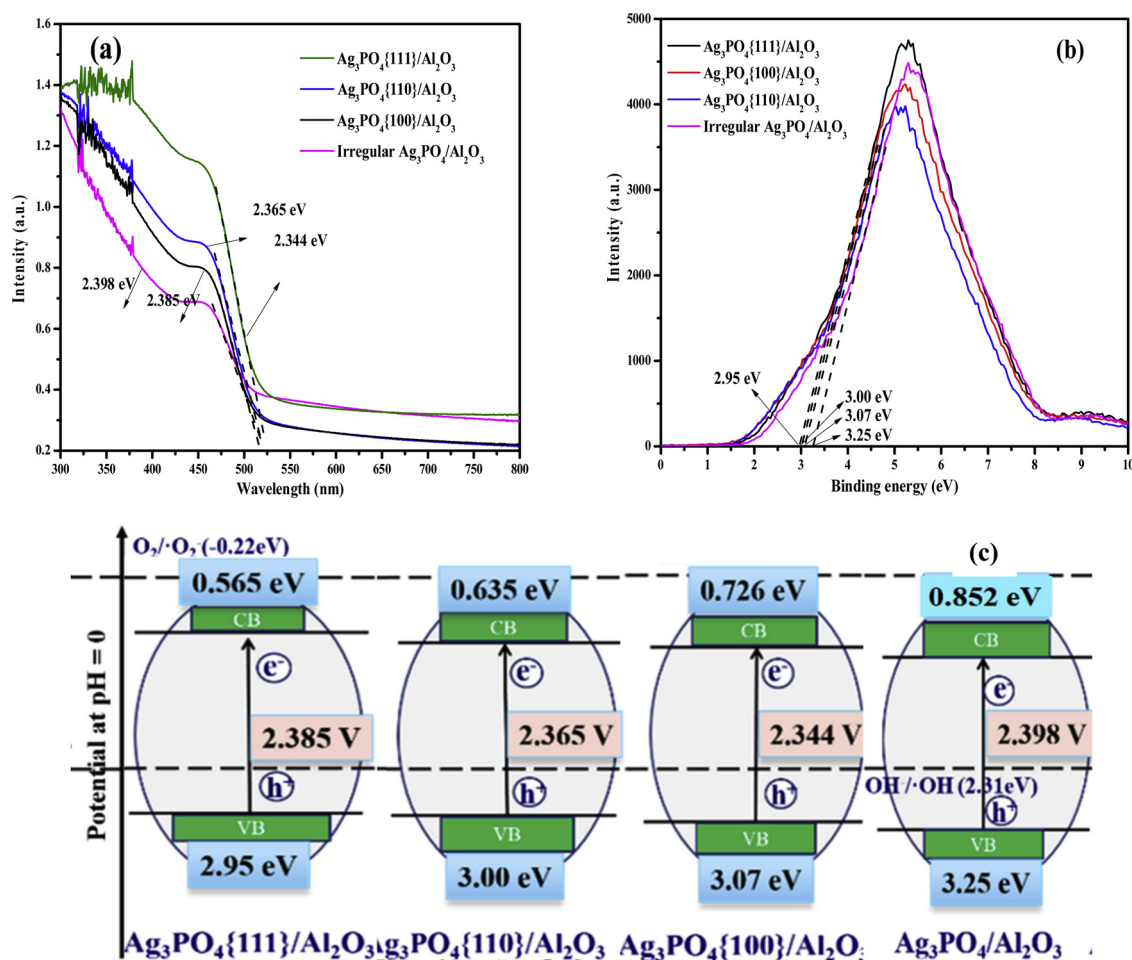


Fig. 4. (a) Ultraviolet-visible diffuse reflectance spectra; (b) Valence-band XPS spectra; and (c) band structure of as-prepared $\text{Ag}_3\text{PO}_4\{111\}/\text{Al}_2\text{O}_3$, $\text{Ag}_3\text{PO}_4\{100\}/\text{Al}_2\text{O}_3$, $\text{Ag}_3\text{PO}_4\{110\}/\text{Al}_2\text{O}_3$, and irregular $\text{Ag}_3\text{PO}_4/\text{Al}_2\text{O}_3$.

system for Ag_3PO_4 deposition, which is also being able to enhance the adsorption of NO molecules and provide more active sites for reaction, thus leading to an accelerated photocatalytic performance. Therefore, the mesoporous Al_2O_3 was chosen as a suitable supporter for Ag_3PO_4 deposition.

The UV-vis absorption spectra of different facet engineered $\text{Ag}_3\text{PO}_4/\text{Al}_2\text{O}_3$ were also determined, as different crystal morphology of Ag_3PO_4 was likely to induce the little shift of absorption edge. As shown in Fig. 4a, the irregular $\text{Ag}_3\text{PO}_4/\text{Al}_2\text{O}_3$ could absorb visible light extended to 517 nm, with a calculated band gap of 2.398 eV, while the adsorption edge of tetrahedral $\text{Ag}_3\text{PO}_4\{111\}/\text{Al}_2\text{O}_3$ was extended to 520 nm, and the direct band gap was estimated to be 2.385 eV. In case of the cubic $\text{Ag}_3\text{PO}_4\{100\}/\text{Al}_2\text{O}_3$ and rhombic dodecahedral $\text{Ag}_3\text{PO}_4\{110\}/\text{Al}_2\text{O}_3$, the absorption edge was drastically shifted to around 524.3 nm and 529 nm, with band gap calculated to be 2.365 eV and 2.344 eV, respectively. Obviously, all the facet engineered $\text{Ag}_3\text{PO}_4/\text{Al}_2\text{O}_3$ samples exhibited a wider visible light adsorption range and thus a smaller band gap than irregular $\text{Ag}_3\text{PO}_4/\text{Al}_2\text{O}_3$. As the narrowed band structure is in favor of the transfer of photogenerated electrons, thereby all the facet engineered $\text{Ag}_3\text{PO}_4/\text{Al}_2\text{O}_3$ may lead to a higher mobility and better photocatalytic activity than irregular $\text{Ag}_3\text{PO}_4/\text{Al}_2\text{O}_3$ [22]. Furthermore, the valence band XPS was also carried out to further analyze the valence band edges for these four samples, as shown in Fig. 4b. The irregular $\text{Ag}_3\text{PO}_4/\text{Al}_2\text{O}_3$ displays a VB maximum energy (E_{VB}) at about 3.25 eV, while the CB minimum energy (E_{CB}) occurs at about 0.852 eV, according to the equation $E_g = E_{\text{VB}} - E_{\text{CB}}$ [31,32]. Similarly, the band structure of $\text{Ag}_3\text{PO}_4\{111\}/\text{Al}_2\text{O}_3$, $\text{Ag}_3\text{PO}_4\{110\}/\text{Al}_2\text{O}_3$, and $\text{Ag}_3\text{PO}_4\{100\}/\text{Al}_2\text{O}_3$ were also estimated, with the E_{CB}

occurred at 0.565 eV, 0.635 eV and 0.726 eV, respectively (Fig. 4c). It can be seen that the $\text{Ag}_3\text{PO}_4\{111\}/\text{Al}_2\text{O}_3$ possess highest VB position and widest band-gap among all these facet engineered $\text{Ag}_3\text{PO}_4/\text{Al}_2\text{O}_3$, which may generate electrons with much higher potential to take part in the photocatalytic reaction.

3.2. Facet-dependent photocatalytic activities of $\text{Ag}_3\text{PO}_4/\text{Al}_2\text{O}_3$

It is well established that adsorption ability of photocatalysts towards the target pollutants is one of the decisive factors affecting the photocatalytic efficiency. The adsorption capacity of the prepared $\text{Ag}_3\text{PO}_4/\text{Al}_2\text{O}_3$ composites for NO was investigated under darkness and shown in Fig. S4. It was observed that the NO adsorption efficiency for $\text{Ag}_3\text{PO}_4\{111\}/\text{Al}_2\text{O}_3$, $\text{Ag}_3\text{PO}_4\{110\}/\text{Al}_2\text{O}_3$, $\text{Ag}_3\text{PO}_4\{100\}/\text{Al}_2\text{O}_3$, irregular $\text{Ag}_3\text{PO}_4/\text{Al}_2\text{O}_3$ were 24%, 19%, 17% and 13% within 6 min, respectively. Obviously $\text{Ag}_3\text{PO}_4\{111\}/\text{Al}_2\text{O}_3$ showed the highest adsorption ability towards NO, which was attributed to that $\text{Ag}_3\text{PO}_4\{111\}/\text{Al}_2\text{O}_3$ had large specific surface area, suitable pore structure and more active sites on its surface. The photocatalytic performance of the as-prepared facet engineered $\text{Ag}_3\text{PO}_4/\text{Al}_2\text{O}_3$ were compared by examining their photocatalytic effects on NO removal under white LED tube irradiation. As shown in Fig. 5a, cubic $\text{Ag}_3\text{PO}_4\{111\}/\text{Al}_2\text{O}_3$ exhibited the highest photocatalytic activity with NO removal efficiency reached 100% after 6 min light irradiation. In contrast, the approximate NO removal efficiency for rhombic dodecahedrons $\text{Ag}_3\text{PO}_4\{110\}/\text{Al}_2\text{O}_3$, tetrahedral $\text{Ag}_3\text{PO}_4\{100\}/\text{Al}_2\text{O}_3$, irregular $\text{Ag}_3\text{PO}_4/\text{Al}_2\text{O}_3$ were 78%, 70%, 52% within same experimental period, respectively. To make a clearly quantitative comparison, the Langmuir-Hinshelwood model (L-

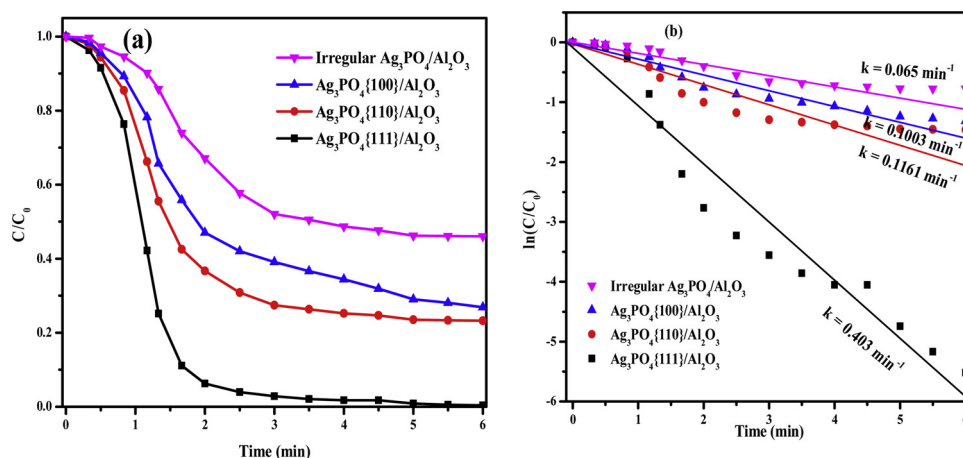


Fig. 5. (a) NO removal efficiency with $\text{Ag}_3\text{PO}_4\{111\}/\text{Al}_2\text{O}_3$, $\text{Ag}_3\text{PO}_4\{110\}/\text{Al}_2\text{O}_3$, $\text{Ag}_3\text{PO}_4\{100\}/\text{Al}_2\text{O}_3$ and irregular $\text{Ag}_3\text{PO}_4/\text{Al}_2\text{O}_3$ and (b) dependence of $\ln(C/C_0)$ vs. irradiation time ($[\text{NO}] = 50 \text{ ppm}$, $V_{\text{Gas}} = 0.15 \text{ L min}^{-1}$).

H) was utilized to fit the curves of photocatalytic removal of NO [10]. Obviously, the initial photocatalytic removal of NO was recognized to follow a first-order kinetics, evidenced by the linear plot of $\ln(C/C_0)$ versus time (t) in Fig. 5b. The normalized NO removal rate of $\text{Ag}_3\text{PO}_4\{111\}/\text{Al}_2\text{O}_3$ is 0.403 min^{-1} , significantly higher than that of $\text{Ag}_3\text{PO}_4\{110\}/\text{Al}_2\text{O}_3$ (0.1161 min^{-1}), $\text{Ag}_3\text{PO}_4\{100\}/\text{Al}_2\text{O}_3$ (0.1003 min^{-1}) and $\text{Ag}_3\text{PO}_4/\text{Al}_2\text{O}_3$ (0.065 min^{-1}). Therefore, it appears that the photocatalytic activity of $\text{Ag}_3\text{PO}_4\{111\}/\text{Al}_2\text{O}_3$ is far superior than that of other facets.

The deviations in the photocatalytic performance of different facet engineered $\text{Ag}_3\text{PO}_4/\text{Al}_2\text{O}_3$ are mainly attributed to the surface structure of Ag_3PO_4 . Therefore, the study of electrochemical impedance spectroscopy (EIS) was conducted to analyze the charge separation ability of

the four $\text{Ag}_3\text{PO}_4/\text{Al}_2\text{O}_3$ samples under light irradiation and dark conditions. As shown in Fig. 6a, the impedance rings of the four $\text{Ag}_3\text{PO}_4/\text{Al}_2\text{O}_3$ electrodes under light irradiation were smaller than that in dark conditions, indicating light irradiation could induce the generation of photoelectron, thus to decrease the impedance for $\text{Ag}_3\text{PO}_4/\text{Al}_2\text{O}_3$ electrodes. Clearly, $\text{Ag}_3\text{PO}_4\{111\}/\text{Al}_2\text{O}_3$ electrode has the minimum impedance ring among all the $\text{Ag}_3\text{PO}_4/\text{Al}_2\text{O}_3$ electrodes under light irradiation, confirming that a more efficient separation of electron-hole pairs and fast interface charge transfer occurs in $\text{Ag}_3\text{PO}_4\{111\}/\text{Al}_2\text{O}_3$ than other $\text{Ag}_3\text{PO}_4/\text{Al}_2\text{O}_3$ electrodes. Moreover, the EIS plots can be fitted with the equivalent circuit inserted in Fig. 6a, consisted of charge transfer resistance (R_2), Warburg impedance (W), capacitance (C), and resistance (R_1). Since the electrolyte and the electrode connection for

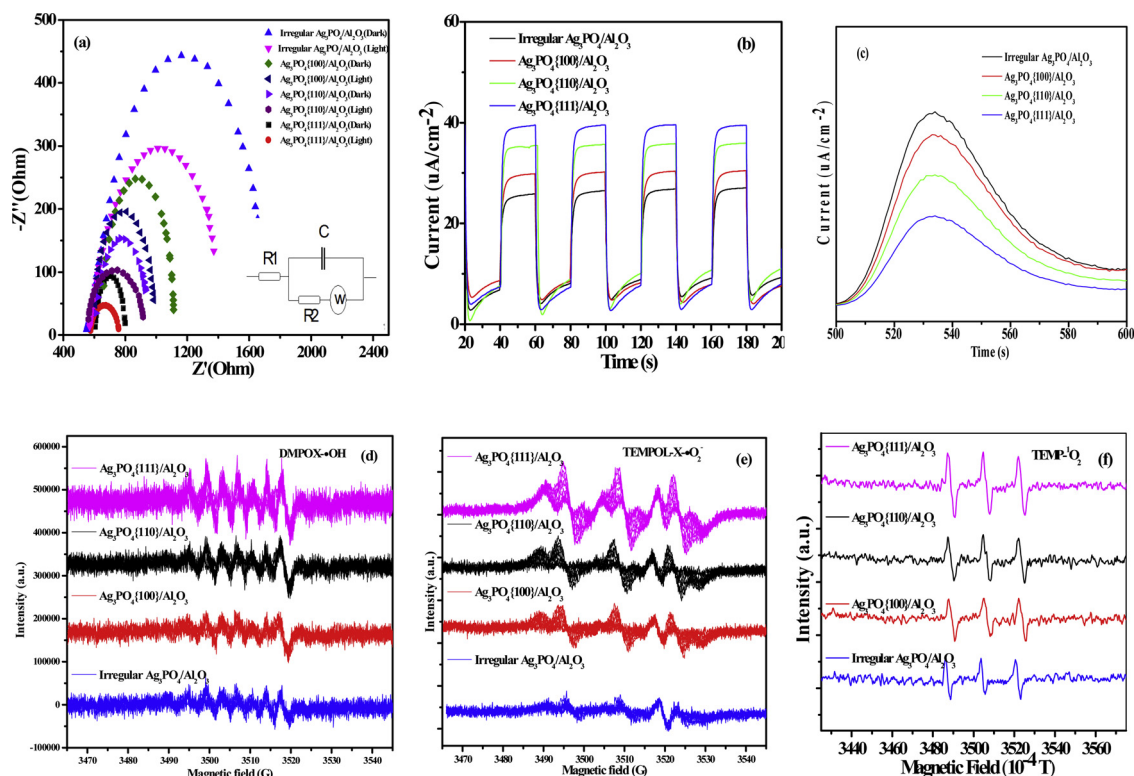


Fig. 6. (a) Nyquist curves in dark and irradiation conditions and (insert) the equivalent circuit used to model the current system, including a component R_1 series resistance, R_2 the charge-transfer resistance, C double layer capacitance, and W Warburg impedance; (b) photocurrent responses, (c) PL spectra and ESR spin-trapping under visible light illumination of (d) DMPO- $\cdot\text{OH}$, (e) TEPOL- $\cdot\text{O}_2^-$ radicals and (f) TEMP- $\cdot\text{O}_2$ for as-prepared $\text{Ag}_3\text{PO}_4\{111\}/\text{Al}_2\text{O}_3$, $\text{Ag}_3\text{PO}_4\{110\}/\text{Al}_2\text{O}_3$, $\text{Ag}_3\text{PO}_4\{100\}/\text{Al}_2\text{O}_3$ and irregular $\text{Ag}_3\text{PO}_4/\text{Al}_2\text{O}_3$.

Table 1

Values of fitting parameters evaluated using equivalent circuit for different facet engineered $\text{Ag}_3\text{PO}_4\{111\}/\text{Al}_2\text{O}_3$, $\text{Ag}_3\text{PO}_4\{110\}/\text{Al}_2\text{O}_3$, $\text{Ag}_3\text{PO}_4\{100\}/\text{Al}_2\text{O}_3$ and irregular $\text{Ag}_3\text{PO}_4/\text{Al}_2\text{O}_3$ electrodes Chi-square values (X_2) $\leq 10^{-4}$.

Experimental processes	R_1 (Ω cm^{-2})	R_2 (Ω cm^{-2})	Total Impedance = $R_1 + R_2$ (Ω cm^{-2})
$\text{Ag}_3\text{PO}_4\{111\}/\text{Al}_2\text{O}_3$ -dark	413	107	520
$\text{Ag}_3\text{PO}_4\{111\}/\text{Al}_2\text{O}_3$ -light	391	68	459
$\text{Ag}_3\text{PO}_4\{110\}/\text{Al}_2\text{O}_3$ -dark	611	297	908
$\text{Ag}_3\text{PO}_4\{110\}/\text{Al}_2\text{O}_3$ -light	607	189	796
$\text{Ag}_3\text{PO}_4\{100\}/\text{Al}_2\text{O}_3$ -dark	660	389	1049
$\text{Ag}_3\text{PO}_4\{100\}/\text{Al}_2\text{O}_3$ -light	604	329	953
Irregular $\text{Ag}_3\text{PO}_4/\text{Al}_2\text{O}_3$ -dark	551	1103	1654
Irregular $\text{Ag}_3\text{PO}_4/\text{Al}_2\text{O}_3$ -light	570	802	1372

measurements of the four $\text{Ag}_3\text{PO}_4/\text{Al}_2\text{O}_3$ samples were the same, therefore, R_1 directly demonstrated the substrate resistance of the determined $\text{Ag}_3\text{PO}_4/\text{Al}_2\text{O}_3$ samples. Through fitting the plots of EIS, R_1 and R_2 for the four $\text{Ag}_3\text{PO}_4/\text{Al}_2\text{O}_3$ samples under dark and VL irradiation were obtained (Table 1). It is obvious that the impedance value of $\text{Ag}_3\text{PO}_4\{111\}/\text{Al}_2\text{O}_3$ (520 Ω cm^{-2} in dark, 459 Ω cm^{-2} under light) was much lower than those of other facet-engineered $\text{Ag}_3\text{PO}_4/\text{Al}_2\text{O}_3$, which is more favorable for charge carrier separation. The charge separation ability of the four $\text{Ag}_3\text{PO}_4/\text{Al}_2\text{O}_3$ samples was also investigated by photocurrent response density data. As shown in Fig. 6b, all the samples exhibited a quick response to the light either on or off. Obviously, the photocurrent of $\text{Ag}_3\text{PO}_4\{111\}/\text{Al}_2\text{O}_3$ electrode was much higher than other $\text{Ag}_3\text{PO}_4/\text{Al}_2\text{O}_3$ electrodes, suggesting $\text{Ag}_3\text{PO}_4\{111\}/\text{Al}_2\text{O}_3$ electrode possessed the optimal carrier separation and transfer efficiency among the four $\text{Ag}_3\text{PO}_4/\text{Al}_2\text{O}_3$ electrodes. Besides, the photoluminescence (PL) spectra of the four $\text{Ag}_3\text{PO}_4/\text{Al}_2\text{O}_3$ samples at an excitation wavelength of 250 nm were measured and presented in Fig. 6c. The $\text{Ag}_3\text{PO}_4\{111\}/\text{Al}_2\text{O}_3$ sample displayed the weakest intensity in the emission of all samples, indicating more efficient separation of photo-generated electron-hole pairs in the $\text{Ag}_3\text{PO}_4\{111\}/\text{Al}_2\text{O}_3$ sample, which was consistent with photocurrent responses and EIS studies. The higher charge separation ability is in favor of improving the photocatalytic activity, thereby $\text{Ag}_3\text{PO}_4\{111\}/\text{Al}_2\text{O}_3$ could obtain the highest photocatalytic activity [25].

To further clarify the surface effect on the photocatalytic properties of the four $\text{Ag}_3\text{PO}_4/\text{Al}_2\text{O}_3$ samples, the differences in radical formation among the four products were also examined. 5,5-dimethyl-1-pyrroline N-oxide (DMPO) spin-trapped electron spin resonance (ESR) spectroscopy was used to monitor the reactive species generated during the photocatalytic process. The results (Fig. 6d) revealed that DMPOX with characteristic seven-line spectra were detected in all the system containing the four $\text{Ag}_3\text{PO}_4/\text{Al}_2\text{O}_3$ samples. DMPOX might originate from the reaction of DMPO with $\cdot\text{OH}$ radicals, suggested by previous report [33]. Theoretically, the photogenerated h^+ of Ag_3PO_4 is thermally favorable to oxidize $\text{OH}^-/\text{H}_2\text{O}$ into $\cdot\text{OH}$, as the oxidation potential of photogenerated h^+ by the four Ag_3PO_4 samples ($\text{VB}_{\{111\}} = 2.95$ eV; $\text{VB}_{\{110\}} = 3.00$ eV; $\text{VB}_{\{100\}} = 3.07$ eV; $\text{VB}_{\text{irregular}} = 3.25$ eV) are much higher than the redox potential of $\cdot\text{OH}/\text{OH}^-$ ($E_0 = 2.8$ V), which is in agreement with the ESR results. Interestingly, the signals are more remarkable for $\text{Ag}_3\text{PO}_4\{111\}/\text{Al}_2\text{O}_3$ than other facet engineered samples, suggesting more $\cdot\text{OH}$ can be generated from $\text{Ag}_3\text{PO}_4\{111\}/\text{Al}_2\text{O}_3$. Moreover, the steady-state $\cdot\text{OH}$ concentration ($[\text{OH}]_{\text{ss}}$) of the four samples was quantified by using pCBA, based on the degradation curves of pCBA in Fig. S5a. As shown in Table 2, $\text{Ag}_3\text{PO}_4\{111\}/\text{Al}_2\text{O}_3$ approximately generate 3.92×10^{-14} M, much higher than other samples, which can well explain the highest photocatalytic activity of $\text{Ag}_3\text{PO}_4\{111\}/\text{Al}_2\text{O}_3$.

$\cdot\text{O}_2^-$ was another important active species for the photocatalytic degradation of NO. Interestingly, the characteristic peak of the TMPOL-

Table 2

Yield of each ROS formation in solution with different facet engineered $\text{Ag}_3\text{PO}_4/\text{Al}_2\text{O}_3$.

Photocatalysts	$[\cdot\text{OH}]_{\text{ss}}$	$[\cdot\text{O}_2^-]_{\text{ss}}$
$\text{Ag}_3\text{PO}_4\{111\}/\text{Al}_2\text{O}_3$	3.92×10^{-14} M	0.52×10^{-9} M
$\text{Ag}_3\text{PO}_4\{110\}/\text{Al}_2\text{O}_3$	2.61×10^{-14} M	0.36×10^{-9} M
$\text{Ag}_3\text{PO}_4\{100\}/\text{Al}_2\text{O}_3$	1.14×10^{-14} M	0.23×10^{-9} M
Irregular $\text{Ag}_3\text{PO}_4/\text{Al}_2\text{O}_3$	1.01×10^{-14} M	0.17×10^{-9} M

X adducts were also observed in the reaction system containing the four $\text{Ag}_3\text{PO}_4/\text{Al}_2\text{O}_3$ samples (Fig. 6e), which might originate from the reaction of TMP with $\cdot\text{O}_2^-$ radicals, suggested by previous reports [34]. However, the photogenerated e^- of Ag_3PO_4 is thermally forbidden to reduce O_2/OH^- into $\cdot\text{O}_2^-/\cdot\text{OOH}$, as the reduction potential of photo-generated e^- by the four Ag_3PO_4 samples ($\text{CB}_{\{111\}} = 0.565$ eV; $\text{CB}_{\{110\}} = 0.635$ eV; $\text{CB}_{\{100\}} = 0.726$ eV; $\text{CB}_{\text{irregular}} = 0.865$ eV) are lower than the redox potential of $\cdot\text{O}_2^-/\text{O}_2$ ($E_0 = -0.22$ eV). Therefore, the generated $\cdot\text{O}_2^-$ may originate from the disproportionate transformation of $\cdot\text{OH}$ [35,36]. In the valence band, absorbed water or hydroxyl groups (OH^-) is initially oxidized by h^+ of Ag_3PO_4 to yield $\cdot\text{OH}$, and then the resulting $\cdot\text{OH}$ combine with each other to form H_2O_2 [35,36]. Subsequently, the generated H_2O_2 can react with $\cdot\text{OH}$ to form protonated superoxide radical ($\cdot\text{HO}_2$) or superoxide radical ($\cdot\text{O}_2^-$) [37,38]. Similarly, nitroblue tetrazolium (NBT, a probe for $\cdot\text{O}_2^-$), was also utilized to quantify the amount of $\cdot\text{O}_2^-$ by the four samples, as indicated by the observation of great decrease in the absorption at 260 nm upon light irradiation in Fig. S5b. Consistent with the ESR analysis, the $[\cdot\text{O}_2^-]_{\text{ss}}$ of $\text{Ag}_3\text{PO}_4\{111\}/\text{Al}_2\text{O}_3$ in Table 2 is 0.52×10^{-9} M, also much higher than other samples. Actually, the highest E_{VB} of $\text{Ag}_3\text{PO}_4\{111\}/\text{Al}_2\text{O}_3$ made the production of $\cdot\text{O}_2^-$ possible via transformation of $\cdot\text{OH}$, and more defects (Raman study in Fig. 2b) could also result in the accelerated e^-h^+ separation, further promoting the reactive species generation for $\text{Ag}_3\text{PO}_4\{111\}/\text{Al}_2\text{O}_3$.

Recently, singlet oxygen ($^1\text{O}_2$) was also often reported as the critical species in photocatalytic process. TEMP was selected as the spin trap to detect $^1\text{O}_2$ in this work. As shown in Fig. 6f, the production of $^1\text{O}_2$ were clearly observed for the four $\text{Ag}_3\text{PO}_4/\text{Al}_2\text{O}_3$ samples with occurrence of three distinctive lines of TEMP- $^1\text{O}_2$ (relative intensities of 1:1:1), since the VB position of $\text{Ag}_3\text{PO}_4/\text{Al}_2\text{O}_3$ samples was positive enough to oxidize O_2 to form $^1\text{O}_2$. In addition, the peak intensities for $\text{Ag}_3\text{PO}_4\{111\}/\text{Al}_2\text{O}_3$ was higher than that of other facet engineered samples, suggesting more $^1\text{O}_2$ can be generated from $\text{Ag}_3\text{PO}_4\{111\}/\text{Al}_2\text{O}_3$ due to higher carrier separation and transfer efficiency.

Thus, the highly-dependent NO removal for the four $\text{Ag}_3\text{PO}_4/\text{Al}_2\text{O}_3$ samples was attributed to different e^-h^+ separation ability and different amounts of generated $\cdot\text{OH}$, $\cdot\text{O}_2^-$ and $^1\text{O}_2$. Especially, $\text{Ag}_3\text{PO}_4\{111\}/\text{Al}_2\text{O}_3$ can photogenerate a higher amount of reactive species than other facets within same period, thereby it can obtain the highest photocatalytic performance. Moreover, each single-crystalline Ag_3PO_4 tetrahedral possesses four highly reactive {111} facets and a high density of corners, edges, and defects, which may markedly increase the number of active sites on their surfaces and facilitate the adsorption of NO molecules on these sites. Therefore, the optimum $\text{Ag}_3\text{PO}_4\{111\}/\text{Al}_2\text{O}_3$ was selected for NO removal, and a series of parameters were also investigated in the following study.

3.3. Surface energies, adsorption of O_2 and H_2O molecule at the exposed facet surface

To further understand the difference of exposed facets of Ag_3PO_4 and its effect on photocatalytic oxidation, we carried out the first-principle calculation using the VASP program, based on density-functional theory (DFT). As shown in Fig. 7, the calculated surface energies of the {111}, {110} and {100} facets are 0.577, 0.289, and 0.343 J/m²,

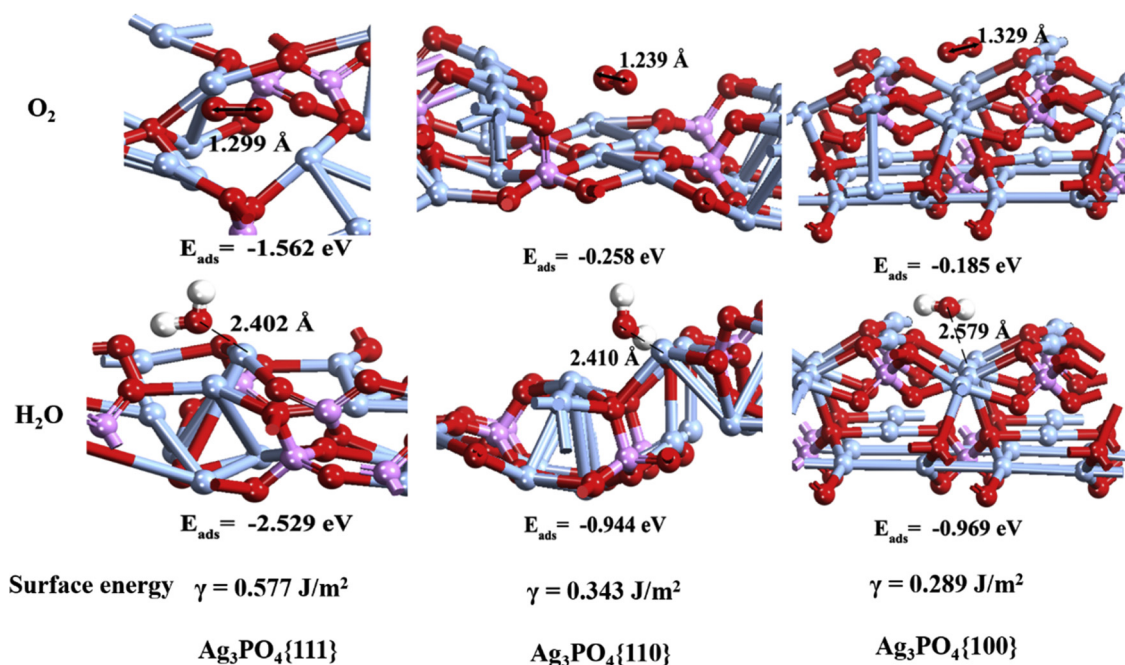


Fig. 7. Adsorption energy of O₂ and H₂O over Ag₃PO₄/Al₂O₃ with different exposed facets. Small red spheres are oxygen, small white spheres are hydrogen, blue spheres are Ag (For interpretation of the references to colour in this figure legend, the reader is referred to the web version of this article).

respectively. According to Wulff construction theory, these facets with high surface energy will vanish in the bulk of crystals as a result of minimizing the total surface energy of crystals [39]. The lower surface energy of {110} and {100} facets are thermodynamically stable facets, probably results from its negligible surface reconstruction and bulk-like structure. While, the high-index {111} facet exhibits the highest surface energies is thermodynamically unstable. In the present case, due to higher stability, lower surface energy, and fewer active sites, {110} and {100} facets are usually less reactive, displaying much poorer performance. It is generally considered that these high energy facets with a higher percentage of under-coordinated atoms are usually more reactive in heterogeneous reactions [40]. Meanwhile, a high density of surface under-coordinated atoms does cause a high surface energy for the crystal facet. Thus, {111} facets with the highest surface energy are usually considered to possess the best performance, which has been proven by the photocatalytic performance.

To understand the different capabilities of the three Ag₃PO₄ in producing oxygen-involved oxidants, the adsorption energies of O₂ and H₂O on the {111}, {110} and {100} facets were also calculated. The capability of a photocatalyst to adsorb O₂/H₂O is critical because only adsorbed O₂/H₂O to the surface of a photocatalyst can capture the photoinduced electrons and then form •OH, which take part directly in photocatalysis or further form •O₂⁻ and H₂O₂ [40]. As shown in Fig. 7, the facets of {100} (-0.185 eV) and {110} (-0.258 eV) exhibit a similar adsorption capacity to molecular O₂ with high energy adsorption, indicating that the adsorption of O₂ over both facets is weak physical adsorption. In contrast, the additional O₂ is strongly bonded with the {111} surface (adsorption energy of -1.562 eV) as the O–O (of adsorbed O₂) bond distance is 1.299 Å. The longer bond length indicates that the bond of O₂ can be more easily broken and activated. Therefore, the strong adsorption of O₂ on {111} facets is energetically more favorable, allowing the {111} facets to produce more •OH/•O₂⁻, thus making them more photocatalytically reactive.

Water always exhibits a cocatalytic effect in many chemical reactions, which play two roles in NO removal; i.e., one is to compensate the consumed hydroxyl group on the catalyst surface and promote the further oxidation of NO intermediates into NO₃, the other is to promote the adsorption and dissolution of NO_x intermediate via hydrogen bond

[41]. Therefore, the adsorption energy of the water molecule with each surface slab is calculated and given in Fig. 7. In general, the H₂O prefers to bond with Ag atoms of all surface slabs, and the adsorption energies of {111}, {110}, and {100} facets are -2.529, -0.944, and -0.969 eV, respectively. It shows that the {111} surface strongly interacted with H₂O, and the additional H₂O is strongly bonded with its surface as the Ag–O (of adsorbed H₂O) bond distance is 2.402 Å. In particular, the short bond length can promote the activation of H₂O molecules by survived h⁺ on the Ag₃PO₄ {111} surface. The easy adsorption and activation of H₂O was favorable for the generation of surface •OH, which can enhance the catalytic oxidation of NO [42]. Because of its higher-water content and better water adsorption ability, Ag₃PO₄ {111} showed excellent activity for NO oxidation.

3.4. Photocatalytic mechanism and conversion pathway of NO oxidation

3.4.1. In situ FT-IR investigation of NO adsorption and transformation pathway

To understand the mechanism of the adsorption and photocatalytic NO oxidation over the Ag₃PO₄ surface, *in situ* DRIFTS is carried out to monitor time-dependent evolution of the reaction intermediates and products. Under dark conditions, a number of adsorption peaks appear after NO are introduced onto the photocatalyst surface. As shown in Fig. 8a, the chemical adsorption and polymerization of NO cause characteristic N₂O₃ (968 cm⁻¹), NO₂ (2080 cm⁻¹), N₂O (2243 and 2280 cm⁻¹) peaks to appear (eqs 6–8) [43]. The disproportionation of NO on the surface of immobilized Ag₃PO₄ was also observed, according to the formation of NO⁻ (1193 and 1142 cm⁻¹), NO⁺ (1690 cm⁻¹), NO₂⁺ (1947 and 2080 cm⁻¹). NO molecules tend to interact with Ag₃PO₄ to form the more stable nitrosyl intermediate. Partial charge transfer from NO to Ag⁺ results in the formation of Ag–NO⁺ and Ag–NO₂⁺. Hence Ag₃PO₄ can be identified as the newly formed active centers to facilitate the activation of NO, which effectively promotes the conversion of NO to the final products by reactive oxygen species. Moreover, the other absorption bands developed progressively can be assigned to the stretching vibration of monodentate (1062 cm⁻¹) and bidentate (1101 cm⁻¹) nitrites, or to bidentate (1012 cm⁻¹), bridging and chelating nitrates (1001 cm⁻¹), or to

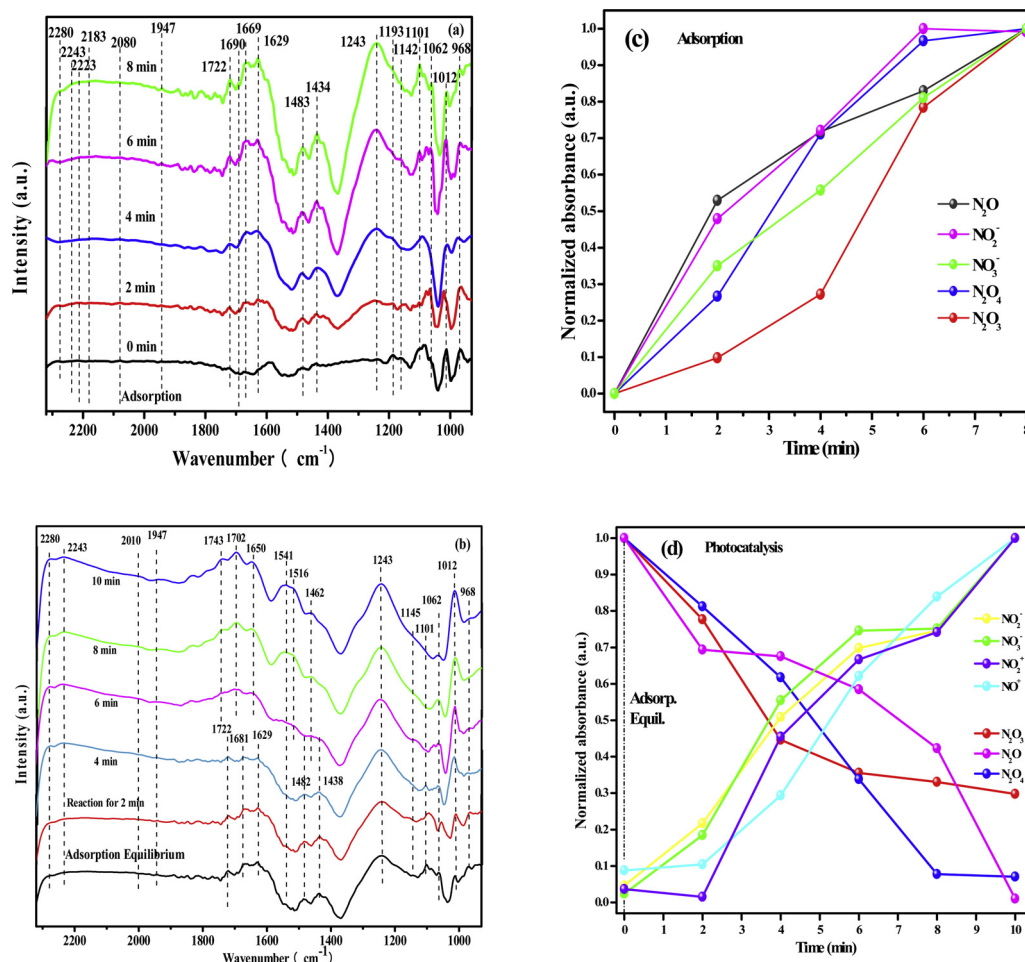
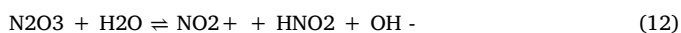


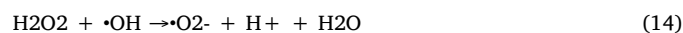
Fig. 8. (a) *in situ* IR spectra of NO adsorption and (b) visible-light reaction processes over $\text{Ag}_3\text{PO}_4\{111\}/\text{Al}_2\text{O}_3$, temporal evolution of normalized absorbance of N species on photocatalysts surface during (c) NO adsorption process and (d) photocatalytic NO oxidation process.

asymmetric stretching ionic nitrate (1483 and 1669 cm^{-1}) [44,45]. The formation of nitrites and nitrates over Ag_3PO_4 during NO adsorption are mainly due to the active Ag atoms of Ag_3PO_4 that facilitate the formation of the activated oxygen species and then enhance the oxidation capacity of the surface oxygen species for NO_x oxidation [46,47]. The normalized absorbance curve clearly shows that the amounts of the NO-related adsorption products like N_2O , N_2O_2 , N_2O_3 and N_2O_4 accumulated on the photocatalyst surface increased with time (Fig. 8c). The adsorption-desorption equilibrium is achieved in 8 min. An adsorption mechanism is proposed, as shown in Eqs. (6 – 12).



After the adsorption, the visible light was involved to activate the photocatalytic reaction. As shown in Fig. 8b, the spectrum of “adsorption” is same as that of “8 min” in the adsorption process. Under visible light irradiation, the enhanced absorption bands of NO^+ (shifted to 1681 cm^{-1}), NO_2^+ (shifted to 1947 and 2010 cm^{-1}) can be observed, suggesting the serious activation and oxidation of NO occurred.

Obviously, the peak intensity at 1062 and 1101 cm^{-1} (nitrite) is significantly decreased with prolonged time, while significant absorption bands at 1438 , 1541 and 1629 cm^{-1} (nitrate ions, NO_3^-) appeared and increased simultaneously, indicating the nitrites were consumed through oxidizing into nitrates on the catalyst surface. It is worth noting that the absorption bands of some adsorption products of N_2O_3 (968 cm^{-1}), N_2O_4 (1722 cm^{-1}), and N_2O (2243 and 2280 cm^{-1}) are increased during the photocatalytic reaction, but the intensity of the peak remained relatively weak, indicating that N_2O , N_2O_3 and N_2O_4 are consumed as they are generated (Eq. 13–19). N_2O , N_2O_3 and N_2O_4 are more toxic than NO as an air pollutant, and thus the conversion of NO into NO_3^- should be largely enhanced to inhibit secondary pollution [48,49]. The normalization absorbance curves in Fig. 8d show that all the NO-related adsorption products can be transformed into a stable final product of nitrates/nitrites by the abundant reactive photo-generated radicals. The results suggest that the $\text{Ag}_3\text{PO}_4\{111\}/\text{Al}_2\text{O}_3$ could transform NO, NO-related adsorption products, and intermediates into the final products of nitrites and nitrates via visible light photocatalysis. Based on these results, the reaction mechanism of photocatalytic NO oxidation by $\text{Ag}_3\text{PO}_4\{111\}/\text{Al}_2\text{O}_3$ is proposed as shown in Eq. (8–14). Both the $\cdot\text{O}_2^-$, $\cdot\text{OH}$ and $^1\text{O}_2$ radicals are involved in the photocatalytic oxidation reactions.



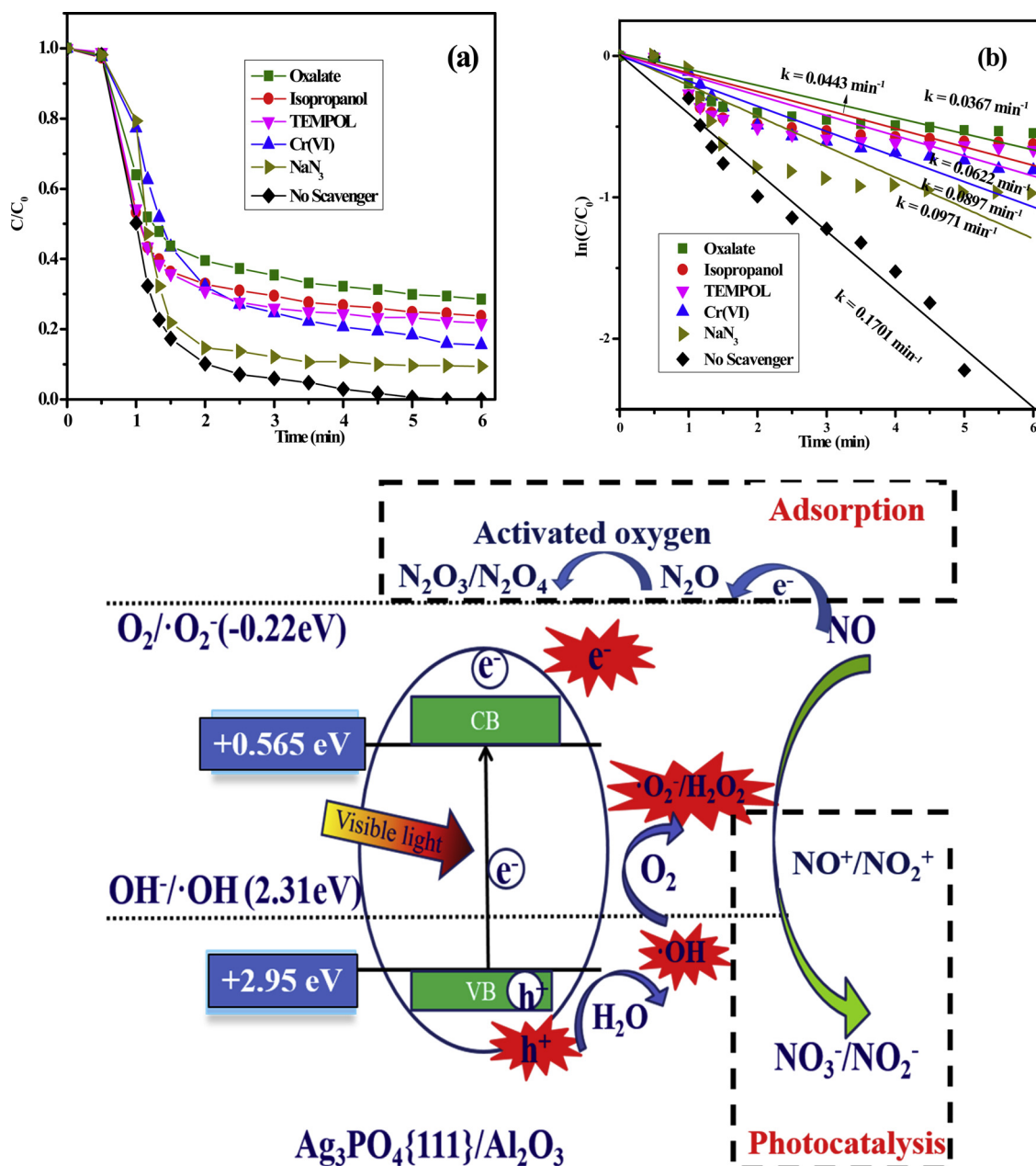
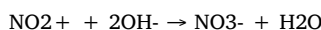
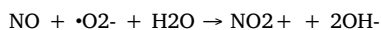
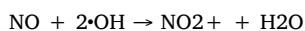
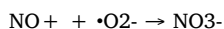
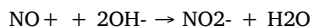


Fig. 9. (a) active species trapping of $\text{Ag}_3\text{PO}_4\{111\}/\text{Al}_2\text{O}_3$ and (b) rate constant; (c) Schematic of charge separation in $\text{Ag}_3\text{PO}_4\{111\}/\text{Al}_2\text{O}_3$ under visible-light irradiation.



3.4.2. Role of reactive species

Reactive species trapping experiments were performed to investigate the role of generated reactive species in the photocatalytic process. In this study, four different chemicals, TEMPOL (a $\cdot\text{O}_2^-$ radical scavenger), isopropanol ($\text{C}_3\text{H}_8\text{O}$, a $\cdot\text{OH}$ radical scavenger), NaN_3 (a $^1\text{O}_2$ radical scavenger), sodium oxalate ($\text{Na}_2\text{C}_2\text{O}_4$, a hole scavenger) and Cr

(VI) ($\text{K}_2\text{Cr}_2\text{O}_7$, a e^- scavenger) were employed. The experimental results (Fig. 9) show that the addition of 1 mM isopropanol greatly inhibited the NO removal efficiency to 31% within 6 min irradiation, indicating $\cdot\text{OH}$ was the crucial active species responsible for NO removal. Meanwhile, the presence of 1 mM TEMPOL had partial limit effect with 23% residual of NO, while the addition of NaN_3 slightly inhibited the NO removal efficiency (from 100% to 90.5%), indicating the moderate role of the generated $\cdot\text{O}_2^-$ and $^1\text{O}_2$. Notably, the introduction of oxalate caused fast deactivation of the $\text{Ag}_3\text{PO}_4\{111\}/\text{Al}_2\text{O}_3$ with 33% residual of NO, indicating that h^+ could directly oxidize NO and played a critical role for NO removal. This is plausible because the E_{VB} (above 2.7 V vs NHE) of $\text{Ag}_3\text{PO}_4\{111\}/\text{Al}_2\text{O}_3$ was more positive than E_0 (NO_2/NO , 1.03 V vs NHE), E_0 (HNO_2/NO , 0.99 V vs NHE), and E_0 (HNO_3/NO , 0.94 V vs NHE) [50,51]. Moreover, as the precursor of $\cdot\text{O}_2^-$ and $\cdot\text{OH}$, the greatly quenched h^+ by oxalate also inhibit the generation of $\cdot\text{O}_2^-$ and $\cdot\text{OH}$, further deactivate the photocatalytic activity of $\text{Ag}_3\text{PO}_4\{111\}/\text{Al}_2\text{O}_3$. Furthermore, adding Cr(VI) also slightly inhibited

the NO removal activity with NO residual of 15%, suggesting that photogenerated electrons did not contribute greatly to NO removal. The current observation is in accordance with ESR analysis, photogenerated h^+ and its derived $\cdot O_2^-$ and $\cdot OH$ rather than photogenerated e^- are greatly involved for NO removal.

In conclusion, the photocatalytic mechanism and conversion pathway of NO oxidation by $Ag_3PO_4\{111\}/Al_2O_3$ can be described in Fig. 9c. Both the conversion pathway of adsorption and photocatalytic NO oxidation are directly reflected in the *in situ* DRIFTS spectra: firstly, NO molecules tend to be adsorbed on Ag_3PO_4 , and the reaction intermediates would be preferentially oxidized by reactive oxygen species, mainly $\cdot O_2^-$ and $\cdot OH$; secondly, Ag_3PO_4 as newly formed active centers facilitate the conversion of adsorbed NO to the final products. Therefore, the present work demonstrates the immobilized facet-engineered Ag_3PO_4 can efficiently transform NO and intermediates to final products via visible light photocatalysis.

3.5. Photocatalytic removal of NO by $Ag_3PO_4\{111\}/Al_2O_3$

3.5.1. Effect of different supporter on NO removal efficiency

To search for an optimum supporter, various mesoporous materials (ZSM-5A, ZSM-4A, zeolite) were also utilized to immobilize $Ag_3PO_4\{111\}$. Similarly, the photocatalytic performances of $Ag_3PO_4\{111\}$ on different supporters were evaluated by NO removal under same conditions. As shown in Fig. 10a, $Ag_3PO_4\{111\}/Al_2O_3$ exhibited the highest NO removal efficiency of 76% within 6 min light irradiation, whereas $Ag_3PO_4\{111\}/ZSM-5A$, $Ag_3PO_4\{111\}/ZSM-4A$, $Ag_3PO_4\{111\}/zeolite$ were 60%, 52%, 29%, respectively. Herein, the rate constant of NO removal over $Ag_3PO_4\{111\}/Al_2O_3$ was calculated to be 0.2769 min^{-1} , much faster than $Ag_3PO_4\{111\}$ deposited on other supporters (Fig. 10b). The excellent performance of Al_2O_3 supporter can

be attributed to its advantages of large surface area ($251.4 \text{ m}^2 \text{ g}^{-1}$), which could load more $Ag_3PO_4\{111\}$ nanoparticles. The exact loading amounts of $Ag_3PO_4\{111\}$ on different supports were quantified by weight determination before and after deposition, which were shown in Table S1. Obviously, mesoporous Al_2O_3 could loading almost 2.23 times amounts of $Ag_3PO_4\{111\}$ than other supporters.

3.5.2. Effect of calcination temperature on NO removal efficiency

Calcination at high temperature, which could induce the changes of physicochemical properties, is an alternative strategy to further enhance the photocatalytic activities of a semiconductor [52]. As shown in Fig. 10c, when the calcination temperature was increased from 0°C to 400°C , the NO removal efficiency over immobilized $Ag_3PO_4\{111\}/Al_2O_3$ was increased from 76% to 100%. Meanwhile, it can be seen that the initial rate constant of NO removal increase from 0.2769 min^{-1} to 0.7294 min^{-1} (Fig. 10d). The increased removal efficiency can be ascribed to the improved crystallinity after calcination, which is beneficial for eliminating bulk traps that act as recombination sites for photo-generated carriers, thus leading to an efficient charge separation. Fig. S6 confirmed that the peak attributed to Ag_3PO_4 increased in intensity and became acute after calcination at 400°C . Moreover, Chong et al. also mentioned that Ag_3PO_4 after calcination could cause oxygen vacancies on Ag_3PO_4 surface, which could create shallow donor states below conduction band and increase the electron concentration, further enhancing the electrical conductivity and increasing active sites [53]. However, when calcination temperature further increased to 500°C , the photocatalytic performance cannot be further elevated and even worse than that of pristine Ag_3PO_4 , with NO removal efficiency decreased to 39% and rate constant became 0.077 min^{-1} . This is mainly due to the decomposition of Ag_3PO_4 nanoparticles (Fig. S6 shows the peak markedly decreases in intensity on calcination at 500°C) and sharply

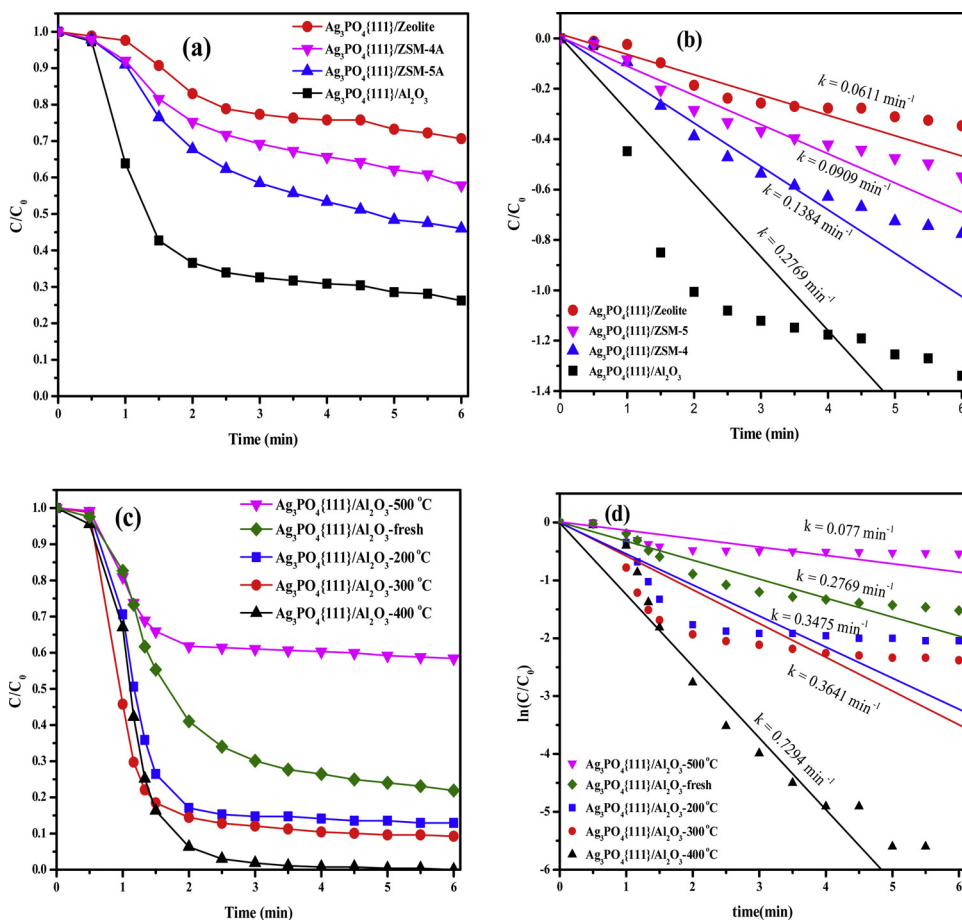


Fig. 10. (a) effect of different supports of $Ag_3PO_4\{111\}$ composites on NO removal rate and (b) dependence of $\ln(C/C_0)$ vs. irradiation time ($[NO] = 50 \text{ ppm}$, $V_{\text{Gas}} = 0.15 \text{ L min}^{-1}$); (c) effect of calcination temperature of $Ag_3PO_4\{111\}/Al_2O_3$ on NO removal rate and (d) dependence of $\ln(C/C_0)$ vs. irradiation time ($[NO] = 50 \text{ ppm}$, $V_{\text{Gas}} = 0.15 \text{ L min}^{-1}$).

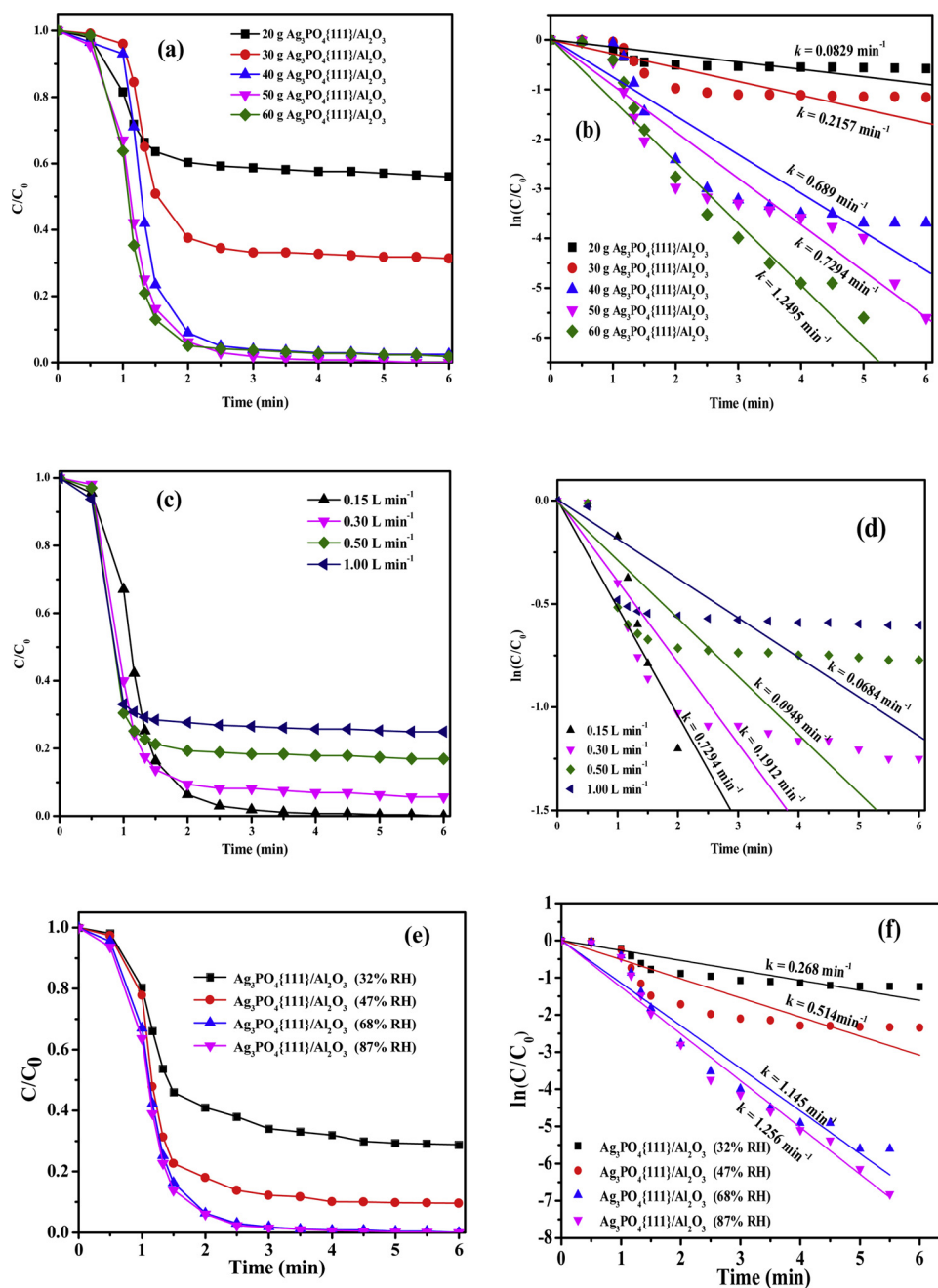


Fig. 11. (a) Effect of $\text{Ag}_3\text{PO}_4\{111\}/\text{Al}_2\text{O}_3$ dosage on NO removal rate and (b) dependence of $\ln(C/C_0)$ vs. irradiation time; (c) Effect of NO inlet velocity on NO removal rate and (d) dependence of $\ln(C/C_0)$ vs. irradiation time; (e) Effect of relative humidity on NO removal rate and (f) dependence of $\ln(C/C_0)$ vs. irradiation time ([NO] = 50 ppm, $V_{\text{Gas}} = 0.15 \text{ L min}^{-1}$).

decreased surface area of Ag_3PO_4 , thus resulted in the great reduction of active sites [54]. Therefore, the suitable temperature of $\text{Ag}_3\text{PO}_4\{111\}/\text{Al}_2\text{O}_3$ in the present system is 400°C .

3.5.3. Effect of $\text{Ag}_3\text{PO}_4\{111\}/\text{Al}_2\text{O}_3$ amount on NO removal efficiency

Fig. 11a shows the removal efficiencies of NO as a function of different dosage of $\text{Ag}_3\text{PO}_4\{111\}/\text{Al}_2\text{O}_3$ under white LED irradiation, ranging from 20 to 60 kg m^{-2} . Obviously, with the increase of $\text{Ag}_3\text{PO}_4\{111\}/\text{Al}_2\text{O}_3$ dosage from 20 to 50 kg m^{-2} filled in the reactor, the photocatalytic removal efficiency of NO was increased from 43.6% to 100% within 6 min light irradiation. Meanwhile, it can be seen that the initial rate constant of NO removal increase from 0.0829 min^{-1} to 0.7294 min^{-1} (Fig. 11b). Herein, the amount of photosensitive $\text{Ag}_3\text{PO}_4\{111\}$ increased with the increase of $\text{Ag}_3\text{PO}_4\{111\}/\text{Al}_2\text{O}_3$

dosage, thus, resulting in a higher photocatalytic activity due to more generation of ROSS. However, with more addition of $\text{Ag}_3\text{PO}_4\{111\}/\text{Al}_2\text{O}_3$ to 60 kg m^{-2} , NO removal efficiency attained an equilibrium and no further remarkable enhancement was observed, which was mainly attributed to that lots of photocatalysts may induce the lower light utilization [55]. Therefore, the optimum dosage of $\text{Ag}_3\text{PO}_4\{111\}/\text{Al}_2\text{O}_3$ in the present system is 40 kg m^{-2} , which can efficiently remove NO with minimum cost of $\text{Ag}_3\text{PO}_4\{111\}/\text{Al}_2\text{O}_3$.

3.5.4. Effect of inlet velocity on NO removal efficiency

The effect of inlet velocity on NO removal efficiencies by $\text{Ag}_3\text{PO}_4\{111\}/\text{Al}_2\text{O}_3$ was also studied, through controlling the inlet velocity of NO varied from 0.15 to 1.00 L min^{-1} . As shown in Fig. 11c, when the inlet velocity increased from 0.15 to 1.00 L min^{-1} , the removal

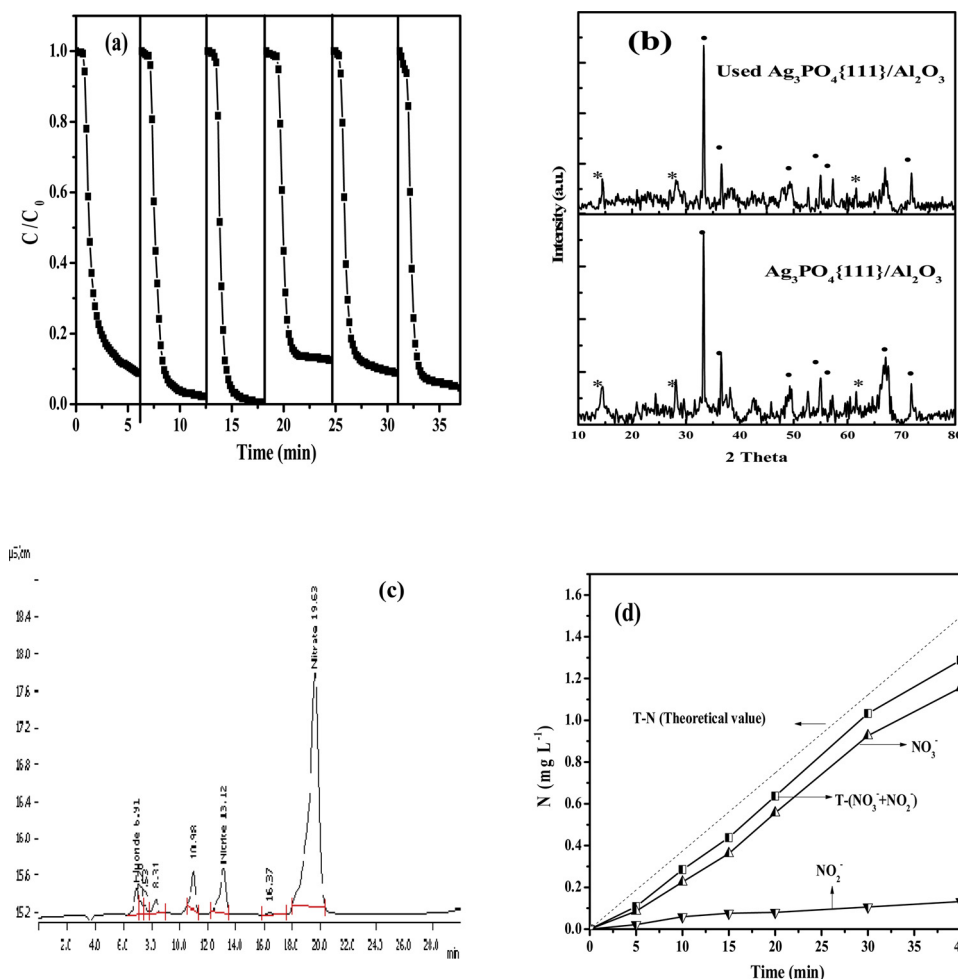


Fig. 12. (a) NO removal efficiency with recycled Ag₃PO₄{111}/Al₂O₃; (b) XRD patterns of fresh Ag₃PO₄{111}/Al₂O₃ and used Ag₃PO₄{111}/Al₂O₃; (c) IC spectrum of NO₃⁻ and NO₂⁻; (d) Amount of NO₃⁻ and NO₂⁻ by extraction with water solution after reaction and detected by IC vs reaction time.

efficiency of NO decreases significantly from 100% to 70%. Meanwhile, it can be seen that the initial rate constant of NO removal decrease from 0.7294 min⁻¹ to 0.0684 min⁻¹ (Fig. 11d). Herein, the increase in the NO flow cause the decrease of NO residence time in the reactor, leading to the fleeing of NO molecular without photocatalytic oxidation, thereby causing the low-efficient performance [56].

3.5.5. Effect of relative humidity on NO removal efficiency

It is necessary to study the effect of relative humidity (RH) on the photocatalytic performance of Ag₃PO₄{111}/Al₂O₃ for further application. Fig. 11e showed the comparison of NO removal efficiency on Ag₃PO₄{111}/Al₂O₃ under white LED irradiation at RH of 30%, 47%, 68% and 89%. Obviously, the photocatalytic removal efficiency of NO was increased from 71.2% to 100% with the rise of RH from 30% to 68%. Meanwhile, it can be seen that the initial rate constant of NO removal increase from 0.268 min⁻¹ to 1.145 min⁻¹ (Fig. 11f). Herein, the increased water molecule can compensate the consumed hydroxyl group on the catalyst surface to produce more •OH radicals from the photo-generated holes and increase NO adsorption via formation of more hydrogen bonds, thus promoting the photocatalytic removal efficiency of NO [41]. However, further increasing RH to 89%, NO removal efficiency was almost stable up, which was mainly attributed to that water molecule reached saturation adsorption on the surface of Ag₃PO₄{111}/Al₂O₃ catalyst. Therefore, Ag₃PO₄{111}/Al₂O₃ exhibited excellent photocatalytic activity for NO removal when relative humidity was higher than or equal to 68%.

3.5.6. Life evaluation of Ag₃PO₄{111}/Al₂O₃ for NO removal

To test the potential applications, the stability and reusability of photocatalysts were checked by conducting multiple runs of NO removal experiments with used Ag₃PO₄{111}/Al₂O₃ under the optimum conditions. As shown in Fig. 12a, Ag₃PO₄{111}/Al₂O₃ exhibits no significant decrease in the photocatalytic activity after six cycles, indicating the Ag₃PO₄{111}/Al₂O₃ was stable and can be used repeatedly. Additionally, Ag₃PO₄{111}/Al₂O₃ after cycling runs were collected and further analyzed by XRD (Fig. 12b). The almost unchanged XRD spectra of Ag₃PO₄{111}/Al₂O₃ before and after the stability test further indicates the phase stability of the Ag₃PO₄{111}/Al₂O₃. To further study the photostability of Ag₃PO₄{111}/Al₂O₃, the used sample after cycling runs was analyzed by XPS spectra. With respect to Ag (Fig.S7), Ag 3d_{5/2} and Ag 3d_{3/2} peaks could be divided into four characteristic peaks, where the divided bands at 367.5 and 373.6 eV indicate the presence of Ag(I), whereas the other two peaks (368.5 and 374.6 eV) suggest the existence of the metallic Ag(0). The XPS result analysis indicated that there was a small amount occurrence of metallic Ag (ca. 0.101%) during photocatalytic reaction process. According to the previous literature, the small amount of metallic Ag could enhance the light absorption due to its SPR effect and improve the separation efficiency of photoinduced electron-hole pairs, thus improving photocatalytic performance of Ag₃PO₄{111}/Al₂O₃ [25]. Moreover, the firmness of Ag₃PO₄{111} loading on the Al₂O₃ support was tested macroscopically by continuous air flowing. The Ag₃PO₄{111}/Al₂O₃ was placed in front of a fan with strong air blowing works for more than 12 h consecutively. It is found that the

weight loss is below 0.061 g, which occupied less than 0.122% of 50 g $\text{Ag}_3\text{PO}_4\{111\}/\text{Al}_2\text{O}_3$. This result indicates that the physicochemical interaction between $\text{Ag}_3\text{PO}_4\{111\}$ and mesoporous Al_2O_3 are strong enough to overcome the continuous air flowing, which could avoid the loss of catalyst particles from the support and reduce the cost of photocatalyst replacement and recovery.

3.5.7. Mass analysis of NO during photocatalytic process with $\text{Ag}_3\text{PO}_4\{111\}/\text{Al}_2\text{O}_3$

These final products accumulated on the photocatalyst surface can be easily removed by water washing and the photocatalyst can be regenerated via this facile method. Meanwhile, the harvested products of NO degradation by $\text{Ag}_3\text{PO}_4\{111\}/\text{Al}_2\text{O}_3$ were quantitatively measured through IC analysis (Fig. 12c). It was found the amount of NO_3^- progressively grew linearly with reaction time and the concentration reached up to 1.166 mg L^{-1} till 40 min, revealing the continuous production of NO_3^- during the photocatalytic process (Fig. 12d). Meanwhile, the amount of NO_2^- slightly increases to 0.134 mg L^{-1} with the prolonged illumination. Notably, the amount of NO_2^- is much lower than that of NO_3^- , indicating that the oxidation of NO and NO_2^- to NO_3^- is the major process and NO_3^- is the major final product. It has been reported that NO_3^- would be accumulated on the surface of $\text{Ag}_3\text{PO}_4\{111\}/\text{Al}_2\text{O}_3$ with proceeded reaction, which would inhibit the ROSs generation and worsen photocatalytic performance in the later stage. However, no significant impact to deactivate $\text{Ag}_3\text{PO}_4\{111\}/\text{Al}_2\text{O}_3$ is primarily attributed to the special mesoporous structure of Al_2O_3 supporter, which could accommodate more products and postpone lifespan. Moreover, the total nitrogen-mass balance between the produced NO_3^- and NO_2^- and the supplied NO was also calculated. It was found that the total amount of NO_x ($\text{NO}_3^- - \text{N} + \text{NO}_2^- - \text{N}$) determined from IC analysis was almost same with that of the supplied NO amount, indicating all gaseous NO was photocatalytically oxidized.

3.6. Conclusions

In conclusion, three different facet-engineered and an irregular $\text{Ag}_3\text{PO}_4/\text{Al}_2\text{O}_3$ samples were synthesized via a wet impregnation-precipitation method. It was confirmed that Ag_3PO_4 nanoparticles with different facet were well dispersed on the surface of mesoporous Al_2O_3 . $\text{Ag}_3\text{PO}_4\{111\}/\text{Al}_2\text{O}_3$ exhibited the highest photocatalytic performance for NO removal, which was mainly attributed to its higher adsorption of O_2 and H_2O , thus to trigger more generation of $\cdot\text{OH}$ and $\cdot\text{O}_2^-$ through DFT calculation and EPR analysis. Moreover, $\text{Ag}_3\text{PO}_4\{111\}/\text{Al}_2\text{O}_3$ maintained high photocatalytic activity in different setting conditions and even the repeated runs without phase changes. A reaction pathway study based on both in situ FT-IR and molecular-level simulation of NO adsorption and transformation indicates that this heterojunction can efficiently transform NO to harmless nitrate products via the $\text{NO} \rightarrow \text{NO}^+$ and $\text{NO}_2^+ \rightarrow \text{nitrate}$ or nitrite routes. The excellent photocatalytic performance of $\text{Ag}_3\text{PO}_4\{111\}/\text{Al}_2\text{O}_3$ is mainly attributed to its high energy facet of $\text{Ag}_3\text{PO}_4\{111\}$, and large BET surface area of Al_2O_3 supporter which are able to improve the molecular transport of reactants and products.

Acknowledgements

The authors wish to thank the National Natural Science Foundation of China (No. 51578556, 21876212, 41603097, 41573086), 21707173 Natural Science Foundation of Guangdong Province (No. 2015A030308005, S2013010012927, S2011010003416), Science and Technology Research Programs of Guangdong Province (No. 2014A020216009), and the Fundamental Research Funds for the Central Universities (No. 13lgjc10) for financially supporting this work. Dr. Xia was also supported by the Start-up Funds for High-Level Talents of Sun Yat-sen University (38000-18821111) and Science and Technology Planning Project of Guangzhou

City (201904010353).

Appendix A. Supplementary data

Supplementary material related to this article can be found, in the online version, at doi:<https://doi.org/10.1016/j.apcatb.2019.117811>.

References

- [1] L.B. Kreuzer, C.K.N. Patel, Nitric oxide air pollution: detection by optoacoustic spectroscopy, *Science* 173 (3991) (1971) 45–47.
- [2] I. Heo, M.K. Kim, S. Sung, I.-S. Nam, B.K. Cho, K.L. Olson, W. Li, Combination of photocatalysis and HC/SCR for improved activity and durability of DeNOx catalysts, *Environ. Sci. Technol.* 47 (8) (2013) 3657–3664.
- [3] Q. Guo, T. Sun, Y. Wang, Y. He, J. Jia, Spray absorption and electrochemical reduction of nitrogen oxides from flue gas, *Environ. Sci. Technol.* 47 (16) (2013) 9514–9522.
- [4] C. Su, X. Ran, J. Hu, C. Shao, Photocatalytic process of simultaneous desulfurization and denitrification of flue gas by TiO_2 –polyacrylonitrile nanofibers, *Environ. Sci. Technol.* 47 (20) (2013) 11562–11568.
- [5] I. Heo, M.K. Kim, S. Sung, I.-S. Nam, B.K. Cho, K.L. Olson, W. Li, Combination of photocatalysis and HC/SCR for improved activity and durability of DeNOx catalysts, *Environ. Sci. Technol.* 47 (8) (2013) 3657–3664.
- [6] F. Dong, Z. Zhao, Y. Sun, Y. Zhang, S. Yan, Z. Wu, An advanced semimetal–organic Bi spheres– $\text{g-C}_3\text{N}_4$ nanohybrid with SPR-enhanced visible-light photocatalytic performance for NO purification, *Environ. Sci. Technol.* 49 (20) (2015) 12432–12440.
- [7] Y. Huang, Y. Liang, Y. Rao, D. Zhu, J. Cao, Z. Shen, W. Ho, S.C. Lee, Environment-friendly carbon quantum dots/ ZnFe_2O_4 photocatalysts: characterization, biocompatibility, and mechanisms for NO removal, *Environ. Sci. Technol.* 51 (5) (2017) 2924–2933.
- [8] F. Dong, Z.Y. Wang, Y.H. Li, W.K. Ho, S.C. Lee, Immobilization of polymeric $\text{g-C}_3\text{N}_4$ on structured ceramic foam for efficient visible light photocatalytic air purification with real indoor illumination, *Environ. Sci. Technol.* 48 (2014) 10345–10355.
- [9] D. Xia, L. Hu, C. He, W. Pan, T. Yang, Y. Yang, D. Shu, Simultaneous photocatalytic elimination of gaseous NO and SO_2 in a $\text{BiOI}/\text{Al}_2\text{O}_3$ -padded trickling scrubber under visible light, *Chem. Eng. J.* 279 (2015) 929–938.
- [10] W. Cui, J. Li, F. Dong, Y. Sun, G. Jiang, W. Cen, S.C. Lee, Z. Wu, Highly efficient performance and conversion pathway of photocatalytic NO oxidation on SrO-Clusters@Amorphous carbon nitride, *Environ. Sci. Technol.* 51 (18) (2017) 10682–10690.
- [11] G. Li, D. Zhang, J.C. Yu, M.K. Leung, An efficient bismuth tungstate visible-light-driven photocatalyst for breaking down nitric oxide, *Environ. Sci. Technol.* 44 (11) (2010) 4276–4281.
- [12] Q. Zhang, Y. Zhou, F. Wang, F. Dong, W. Li, H.M. Li, G.R. Patzke, From semiconductors to semimetals: bismuth as a photocatalyst for NO oxidation in air, *J. Mater. Chem. A Mater. Energy Sustain.* 2 (2014) 11065–11072.
- [13] S. Ge, L. Zhang, Efficient visible light driven photocatalytic removal of RhB and NO with low temperature synthesized $\text{In}(\text{OH})\text{XSy}$ hollow nanocubes: a comparative study, *Environ. Sci. Technol.* 45 (7) (2011) 3027–3033.
- [14] R. Sugranea, J. Balbuena, M. Cruz-Yusta, F. Martin, J. Morales, L. Sanchez, Efficient behavior of hematite towards the photocatalytic degradation of NOx gases, *Appl. Catal. B* 165 (2015) 529–536.
- [15] F. Dong, Z.W. Zhao, Y.J. Sun, Y.X. Zhang, S. Yan, Z.B. Wu, An advanced semimetal-organic spheres– $\text{g-C}_3\text{N}_4$ nanohybrid with SPR-enhanced visible-light photocatalytic performance for NO purification, *Environ. Sci. Technol.* 49 (2015) 12432–12440.
- [16] F. Teng, Z.L. Liu, A. Zhang, Facile synthesis of polypod-like Ag_3PO_4 particles and its application in pollutant degradation under natural indoor week light irradiation, *Environ. Sci. Technol.* 49 (16) (2015) 9489–9494.
- [17] H. Wang, L. He, L.H. Wang, P.F. Hu, L. Guo, X.D. Han, J.H. Li, Facile synthesis of Ag_3PO_4 tetrapod microcrystals with an increased percentage of exposed {110} facets and highly efficient photocatalytic properties, *Cryst. Eng. Comm.* 14 (2012) 8342–8344.
- [18] Z.G. Yi, J.H. Ye, N. Kikugawa, T. Kako, S.X. Ouyang, H.S. Williams, H. Yang, J.Y. Cao, W.J. Luo, Z.S. Li, Y. Liu, R.L. Withers, An orthophosphate semiconductor with photooxidation properties under visible-light irradiation, *Nat. Mater.* 9 (2010) 559–564.
- [19] Z.B. Jiao, Y. Zhang, H.C. Yu, G.X. Lu, J.H. Ye, Y.P. Bi, Concave trisoctahedral Ag_3PO_4 microcrystals with high-index facets and enhanced photocatalytic properties, *Chem. Commun. (Camb.)* 308 (49) (2013) 636–638.
- [20] Y.P. Bi, S.X. Ouyang, N. Umezawa, J.Y. Cao, J.H. Ye, Facet effect of single-crystalline Ag_3PO_4 sub-microcrystals on photocatalytic properties, *J. Am. Chem. Soc.* 133 (2011) 6490–6492.
- [21] D.J. Martin, N. Umezawa, X.W. Chen, J.H. Ye, J.W. Tang, Facet engineered Ag_3PO_4 for efficient water photooxidation, *Energy Environ. Sci.* 6 (2013) 3380–3386.
- [22] B.J. Zheng, X. Wang, C. Liu, K. Tan, Z.X. Xie, L.S. Zheng, High-efficiently visible light-responsive photocatalysts: Ag_3PO_4 tetrahedral microcrystals with exposed {111} facets of high surface energy, *J. Mater. Chem. A Mater. Energy Sustain.* 1 (2013) 12635–12640.
- [23] D. Xia, Z.R. Shen, G.C. Huang, W.J. Wang, J.C. Yu, P.K. Wong, Red phosphorus: an earth-abundant elemental photocatalyst for “Green” bacterial inactivation under visible light, *Environ. Sci. Technol.* 49 (2015) 6264–6273.
- [24] D. Xia, T.W. Ng, T. An, G. Li, Y. Li, H.Y. Yip, H. Zhao, A. Lu, P.K. Wong, A recyclable

- mineral catalyst for visible-light-driven photocatalytic inactivation of bacteria: natural magnetic sphalerite, *Environ. Sci. Technol.* 47 (2013) 11166–11173.
- [25] D.H. Xia, L.L. Hu, X.Q. Tan, C. He, W.Q. Pan, T.S. Yang, Y.L. Huang, D. Shu, Immobilization of self-stabilized plasmonic Ag-AgI on mesoporous Al_2O_3 for efficient purification of industrial waste gas with indoor LED illumination, *Appl. Catal. B* 185 (2016) 295–306.
- [26] D.H. Xia, T.C. An, G.Y. Li, W.J. Wang, H.J. Zhao, P.K. Wong, Synergistic photocatalytic inactivation mechanisms of bacterial by graphene sheets grafted plasmonic Ag-AgX (X = Cl, Br, I) composite photocatalyst under visible light irradiation, *Water Res.* 99 (2016) 149–161.
- [27] B. Liu, Z.Y. Li, S. Xu, D.D. Han, D.Y. Lu, Enhanced visible-light photocatalytic activities of $\text{Ag}_3\text{PO}_4/\text{MWCNT}$ nanocomposites fabricated by facile in situ precipitation method, *J. Alloys. Compd.* 596 (2014) 19–24.
- [28] Q.J. Xiang, D. Lang, T.T. Shen, F. Liu, Graphene-modified nanosized Ag_3PO_4 photocatalysts for enhanced visible-light photocatalytic activity and stability, *Appl. Catal. B* 162 (2015) 196–203.
- [29] D. Wu, B. Wang, W. Wang, T.C. An, G.Y. Li, T.W. Ng, H.Y. Yip, C.M. Xiong, H.K. Lee, P.K. Wong, Visible-light-driven BiOBr nanosheets for highly facet-dependent photocatalytic inactivation of *Escherichia coli*, *J. Mater. Chem. A Mater. Energy Sustain.* 3 (2015) 15148–15155.
- [30] X. Guan, L. Guo, Cocatalytic effect of SrTiO_3 on Ag_3PO_4 toward enhanced photocatalytic water oxidation, *ACS Catal.* 4 (2014) 3020–3026.
- [31] M. Pan, H. Zhang, G. Gao, L. Liu, W. Chen, Facet-dependent catalytic activity of nanosheet-assembled bismuth oxyiodide microspheres in degradation of bisphenol A, *Environ. Sci. Technol.* 49 (2015) 6240–6248.
- [32] Y. Bi, S. Ouyang, J. Cao, J. Ye, Facile synthesis of rhombic dodecahedral $\text{AgX}/\text{Ag}_3\text{PO}_4$ (X = Cl, Br, I) heterocrystals with enhanced photocatalytic properties and stabilities, *Phys. Chem. Chem. Phys.* 13 (2011) 10071–10075.
- [33] W.-S. Wang, H. Du, R.-X. Wang, T. Wen, A.-W. Xu, Heterostructured $\text{Ag}_3\text{PO}_4/\text{AgBr}$ /Ag plasmonic photocatalyst with enhanced photocatalytic activity and stability under visible light, *Nanoscale* 5 (2013) 3315–3321.
- [34] J. Lin, M. Guo, C.T. Yip, W. Lu, G. Zhang, X. Liu, High temperature crystallization of free-standing anatase TiO_2 nanotube membranes for high efficiency dye-sensitized solar cells, *Adv. Funct. Mater.* 23 (2013) 5952–5960.
- [35] W. Wang, Y. Yu, T. An, G. Li, H.Y. Yip, J.C. Yu, P.K. Wong, Visible-light-driven photocatalytic inactivation of *E. Coli* K-12 by bismuth vanadate nanotubes: bactericidal performance and mechanism, *Environ. Sci. Technol.* 46 (2012) 4599–4606.
- [36] K.T. Ranjit, I. Willner, S.H. Bossmann, A.M. Braun, Lanthanide oxide-doped titanium dioxide photocatalysts: novel photocatalysts for the enhanced degradation of p-chlorophenoxyacetic acid, *Environ. Sci. Technol.* 35 (2001) 1544–1549.
- [37] Y. Pan, H. Su, Y. Zhu, H.V. Molamahmood, M. Long, CaO_2 based Fenton-like reaction at neutral pH: accelerated reduction of ferric species and production of superoxide radicals, *Water Res.* 145 (2018) 731–740.
- [38] A.G. Rincon, C. Pulgarin, Effect of pH, inorganic ions, organic matter and H_2O_2 on *E. Coli* K12 photocatalytic inactivation by TiO_2 : implications in solar water disinfection, *Appl. Catal. B* 51 (2004) 283–302.
- [39] H. Li, H. Shang, X. Cao, Z. Yang, Z. Ai, L. Zhang, Oxygen vacancies mediated complete visible light NO oxidation via side-on bridging superoxide radicals, *Environ. Sci. Technol.* 52 (2018) 8659–8665.
- [40] S. Rong, P. Zhang, F. Liu, Y. Yang, Engineering crystal facet of $\alpha\text{-MnO}_2$ nanowire for highly efficient catalytic oxidation of carcinogenic airborne formaldehyde, *ACS Catal.* 8 (2018) 3435–3446.
- [41] C.B. Zhang, Y.B. Li, Y.F. Wang, H. He, Sodium-promoted Pd/TiO_2 for catalytic oxidation of formaldehyde at ambient temperature, *Environ. Sci. Technol.* 48 (2014) 5816–5822.
- [42] H. Wang, Y. Sun, G. Jiang, Y. Zhang, H. Huang, Z. Wu, S.C. Lee, F. Dong, Unraveling the mechanisms of visible light photocatalytic NO purification on earth-abundant insulator-based core-shell heterojunctions, *Environ. Sci. Technol.* 52 (3) (2018) 1479–1487.
- [43] G. Dong, W.K. Ho, L. Zhang, Photocatalytic NO removal on BiOI surface: the change from nonselective oxidation to selective oxidation, *Appl. Catal. B* 168–169 (2015) 490–496.
- [44] J. Ma, H. Wu, Y. Liu, H. He, Photocatalytic removal of NO_x over visible light responsive oxygen-deficient TiO_2 , *J. Phys. Chem. C* 118 (14) (2014) 7434–7441.
- [45] X. Song, Y. Hu, M. Zheng, C. Wei, Solvent-free in situ synthesis of $\text{g-C}_3\text{N}_4/\{001\}\text{TiO}_2$ composite with enhanced UV- and visible-light photocatalytic activity for NO oxidation, *Appl. Catal. B* 182 (2016) 587–597.
- [46] W.K. Ho, Z. Zhang, M. Xu, X. Zhang, X. Wang, Enhanced visible-light-driven photocatalytic removal of NO: effect on layer distortion on $\text{g-C}_3\text{N}_4$ by H_2 heating, *Appl. Catal. B* 179 (2015) 106–112.
- [47] W. Cui, J. Li, W. Cen, Y. Sun, S.C. Lee, F. Dong, Steering the interlayer energy barrier and charge flow via bi-oriented transportation channels in $\text{g-C}_3\text{N}_4$: enhanced photocatalysis and reaction mechanism, *J. Catal.* 352 (2017) 351–360.
- [48] G. Jiang, X. Li, M. Lan, T. Shen, X. Lv, F. Dong, S. Zhang, Monodisperse bismuth nanoparticles decorated graphitic carbon nitride: enhanced visible-light-response photocatalytic NO removal and reaction pathway, *Appl. Catal. B* 205 (2017) 532–540.
- [49] D. Zhang, M. Wen, S. Zhang, P. Liu, Z. Wei, G. Li, H. Li, Au nanoparticles enhanced rutile TiO_2 nanorod bundles with high visible-light photocatalytic performance for NO oxidation, *Appl. Catal. B-Environ.* 147 (8) (2014) 610–616.
- [50] J. Li, X. Dong, Y. Sun, W. Cen, F. Dong, Facet-dependent interfacial charge separation and transfer in plasmonic photocatalysts, *Appl. Catal. B* 226 (2018) 269–277.
- [51] G. Dong, L. Yang, F. Wang, L. Zang, C. Wang, Removal of nitric oxide through visible light photocatalysis by $\text{g-C}_3\text{N}_4$ modified with perylene imides, *ACS Catal.* 6 (10) (2016) 6511–6519.
- [52] D. Xia, W. Xu, Y. Wang, J. Yang, Y. Huang, L. Hu, C. He, D. Shu, D.Y.C. Leung, Z. Pang, Enhanced performance and conversion pathway for catalytic ozonation of methyl mercaptan on single-atom Ag deposited three-dimensional ordered mesoporous MnO_2 , *Environ. Sci. Technol.* 52 (22) (2018) 13399–13409.
- [53] R. Chong, X. Cheng, B. Wang, D. Li, Z. Chang, L. Zhang, Enhanced photocatalytic activity of Ag_3PO_4 for oxygen evolution and methylene blue degradation: effect of calcination temperature, *Int. J. Hydrogen Energy* 41 (2016) 2575–2582.
- [54] D. Zhang, M. Wen, S. Zhang, P. Liu, Z. Wei, G. Li, H. Li, Au nanoparticles enhanced rutile TiO_2 nanorod bundles with high visible light photocatalytic performance for NO oxidation, *Appl. Catal. B* 147 (8) (2014) 610–616.
- [55] X. Ding, W. Ho, J. Shang, L. Zhang, Self doping promoted photocatalytic removal of NO under visible light with Bi_2MoO_6 : indispensable role of superoxide ions, *Appl. Catal. B-Environ.* 182 (2016) 316–325.
- [56] W. Cui, J. Li, W. Cen, Y. Sun, S.C. Lee, F. Dong, Steering the interlayer energy barrier and charge flow via bi-oriented transportation channels in $\text{g-C}_3\text{N}_4$: enhanced photocatalysis and reaction mechanism, *J. Catal.* 352 (2017) 351–360.